


















The GALAH survey: tracing the Milky Way’s formation and evolution through RR Lyrae stars

Valentina D’Orazi ^{1,2,3,4}★, Nicholas Storm ⁵, Andrew R. Casey ^{3,4}, Vittorio F. Braga ⁶, Alice Zocchi,⁷ Giuseppe Bono,^{1,6}★ Michele Fabrizio,^{6,8} Christopher Sneden,⁹ Davide Massari,¹⁰ Riano E. Giribaldi,¹¹ Maria Bergemann ⁵, Simon W. Campbell,^{3,4} Luca Casagrande ^{4,12}, Richard de Grijs,^{13,14,15} Gayandhi De Silva,^{4,13} Maria Lugaro,^{3,16,17,18} Daniel B. Zucker,^{4,13} Angela Bragaglia,¹⁰ Diane Feuillet ¹⁹, Giuliana Fiorentino ⁶, Brian Chaboyer,²⁰ Massimo Dall’Ora,²¹ Massimo Marengo,²² Clara E. Martínez-Vázquez ²³, Noriyuki Matsunaga,^{24,25} Matteo Monelli ^{6,26,27}, Joseph P. Mullen,²⁸ David Nataf,²⁹ Maria Tantalo,^{6,26,27} Frederic Thevenin ³⁰, Fabio R. Vitello,³¹ Rolf-Peter Kudritzki,^{32,33} Joss Bland-Hawthorn ^{4,34}, Sven Buder ^{4,12}, Ken Freeman,^{4,12} Janez Kos ³⁵, Geraint F. Lewis ³⁴, Karin Lind,³⁶ Sarah Martell ^{4,37}, Sanjib Sharma,^{4,34} Dennis Stello^{4,34,37} and Tomaž Zwitter ³⁵

Affiliations are listed at the end of the paper

Accepted 2024 April 26. Received 2024 April 25; in original form 2024 March 19

ABSTRACT

Stellar mergers and accretion events have been crucial in shaping the evolution of the Milky Way (MW). These events have been dynamically identified and chemically characterized using red giants and main-sequence stars. RR Lyrae (RRL) variables can play a crucial role in tracing the early formation of the MW since they are ubiquitous, old ($t \geq 10$ Gyr) low-mass stars and accurate distance indicators. We exploited Data Release 3 of the GALAH survey to identify 78 field RRLs suitable for chemical analysis. Using synthetic spectra calculations, we determined atmospheric parameters and abundances of Fe, Mg, Ca, Y, and Ba. Most of our stars exhibit halo-like chemical compositions, with an iron peak around $[\text{Fe}/\text{H}] \approx -1.40$, and enhanced Ca and Mg content. Notably, we discovered a metal-rich tail, with $[\text{Fe}/\text{H}]$ values ranging from -1 to approximately solar metallicity. This sub-group includes almost 1/4 of the sample, it is characterized by thin disc kinematics and displays sub-solar α -element abundances, marginally consistent with the majority of the MW stars. Surprisingly, they differ distinctly from typical MW disc stars in terms of the s-process elements Y and Ba. We took advantage of similar data available in the literature and built a total sample of 535 field RRLs for which we estimated kinematical and dynamical properties. We found that metal-rich RRLs (1/3 of the sample) likely represent an old component of the MW thin disc. We also detected RRLs with retrograde orbits and provided preliminary associations with the Gaia–Sausage–Enceladus, Helmi, Sequoia, Sagittarius, and Thamnos stellar streams.

Key words: stars: abundances – stars: Population II – stars: variables: RR Lyrae – Galaxy: abundances – Galaxy: disc – Galaxy: halo.

1 INTRODUCTION

RR Lyrae stars (RRLs) play a crucial role in our understanding of the Universe. In the foundational review of the field, Preston (1964) articulated that these stars act as essential tools in unravelling the evolutionary processes that shaped our Galaxy. Through their unique characteristics and patterns, RRLs provide insights into the age, structure, and formation history of our Milky Way (MW; e.g. Dékány et al. 2013; Belokurov et al. 2018). A wealth of studies have leveraged the insights provided by RRLs to delve into the chemical and dynamical transformations characterizing the MW evolutionary

journey (see e.g. For, Sneden & Preston 2011; Hansen et al. 2016; Crestani et al. 2021a, b; Fabrizio et al. 2021, Ablimit et al. 2022; Li & Binney 2022 and references therein).

RRLs are low-mass, old (≈ 10 Gyr) stars that reside on the horizontal branch, undergoing core helium burning, and are characterized by their pulsations within the instability strip, with typical periods shorter than one day (Bono et al. 2011; Marconi 2012). They are radial variables oscillating in the fundamental mode (RRab), in the first overtone (RRc), and mixed-mode (RRd, two modes are simultaneously excited), which offer valuable insights into the physics of stellar evolution and pulsation (e.g. Catelan 2007, Soszyński et al. 2011).

Dating back to the works of Baade (1958) and Sandage (1962), RRL stars were identified as reliable standard candles because their

* E-mail: valentina.dorazi@inaf.it (VD); giuseppe.bono@inaf.it (GB)

absolute visual magnitude is inversely related to their metallicity. The precision of using RRL stars as distance indicators significantly improved with the discovery that they adhere to well-defined Period–Luminosity (PL) relations for wavelengths exceeding the R band as detailed by (Longmore et al. 1989; Bono et al. 2011; Braga et al. 2021). This means that they are invaluable tools for distance determination within our Galaxy and beyond (Neeley et al. 2019; Latham, Kamenetzky & Fitzgerald 2023 and references therein). With this capability, distances can be easily determined with a remarkable level of precision better than 5 percent (see Beaton et al. 2018 for a review). Owing to their distinct pulsation patterns and relatively high luminosity, this class of variable stars stands out in time-domain surveys, serving as indispensable tools for probing diverse structures in our Galaxy (Bhardwaj 2024; Clementini 2024). As a result, RRLs serve as pivotal markers for uncovering the formation of Galactic substructures and potential merger events, as exemplified by the sample of nine RRLs in Feuillet et al. (2022) and the deduced accreted origin from their (low) aluminium content.

While there has been considerable research on the metallicities of RR Lyrae stars (recent works including Liu et al. 2013; Fabrizio et al. 2019; Gilligan et al. 2021) the field remains limited in terms of high-resolution spectroscopic studies that delve into their detailed chemical abundances. Crestani et al. (2021b) conducted the most extensive high-resolution spectroscopic analysis of RR Lyrae stars to date. Their sample covered 162 stars, with an additional 46 obtained from online archival repositories. The data set encompassed a diverse range of spectral sources, including UVES, HARPS, and FEROS at ESO, HRS at SALT and *echelle* at DuPont. Using the PYTHON wrapper `pymooji` (Adamow 2017)¹ of the 2019 version of MOOG (Snedden 1973) and adopting the LTE assumption. These authors derived abundances for Fe, Mg, and Ca through equivalent width (EW) methods. Notably, this work represents a significant milestone as it marks the detection of subsolar $[\alpha/\text{Fe}]$ ² ratios in old stellar tracers based on a large sample of stars, as previously introduced by Prudil et al. (2020). Crestani and collaborators found a resemblance in the trend of $[\alpha/\text{Fe}]$ with metallicity between α -poor, metal-rich RR Lyrae stars and red giants (RGs) in the Sagittarius dwarf galaxy, as well as between α -enhanced, metal-poor RR Lyrae stars and RGs in ultra-faint dwarf (UDF) galaxies. Instead, Prudil et al. (2020), utilizing kinematic evidence, asserted that the metal-rich, α -poor RRL population genuinely belongs to the Galactic disc. Yet, this introduces a dilemma. The age of the thin disc is less than ≈ 8 Gyr (Kilic et al. 2017), while RRLs are understood to exceed 10 Gyr in age. On the other hand, their chemical composition does not align with the predominant makeup of the Galactic thick disc (which is α -rich), suggesting that they must represent an exceptionally α -poor segment of the thick disc (Prudil et al. 2020).

We used the DR3 of the GALAH survey (GALactic Archeology with Hermes, De Silva et al. 2015; Buder et al. 2021) and identified a sample of 78 RRL stars, suitable for chemical analysis. We provide atmospheric parameters and detailed abundance values for iron (Fe), α -elements (Mg, Si, Ca), and n -capture elements (Y, Ba). This represents the most extensive high-resolution, single-source data base of detailed abundance determinations for RRLs in the current literature. The organisation of the paper is structured in the following

¹This code is developed and maintained by M. Adamow and can be downloaded at <https://github.com/madamow/pymooji>.

²We adopt the standard spectroscopic notation such that $[\text{Fe}/\text{H}] = \log \left(\frac{N_{\text{Fe}}}{N_{\text{H}}} \right)_{\star} - \log \left(\frac{N_{\text{Fe}}}{N_{\text{H}}} \right)_{\odot}$ and $[\text{X}/\text{Fe}] = [\text{X}/\text{H}] - [\text{Fe}/\text{H}]$ for a given species X. Units are in dex.

manner: Section 2 introduces the sample and discusses the pulsation properties of the RRL stars examined in this study. Section 3 details the methodology of the abundance analysis. The findings related to chemistry, kinematics and dynamics are presented and explored in Sections 4 and 5. In Section 6, we discuss the scientific implications of our findings; finally, Section 7 concludes the paper by summarizing the key results.

2 RRL SAMPLE AND PULSATION PROPERTIES

We began our study with a catalogue of RR Lyrae stars, assembled over the past few years (Fabrizio et al. 2019, 2021; Braga et al. 2021). The foundation of the catalogue is built upon *Gaia* DR3 (Gaia Collaboration et al. 2023) and its comprehensive catalogue of RRL stars, as detailed in Clementini et al. (2023), but it includes RRLs from almost all the known photometric surveys (Catalina, Drake et al. 2009, 2017; ASAS; Pojmanski 1997; ASAS-SN; Jayasinghe et al. 2019 to name a few, see Braga et al. 2021; Fabrizio et al. 2021 for the details). The catalogue contains 286 135 RRLs, all of which have a valid *Gaia* DR3 source id, despite not all of them being in the `gaiadr3.vari_rrlyrae` table on the ESA archive³. As already discussed in Braga et al. (2021), for 10 413 of them, we have associated spectra, but only for a minority (192), we have high-resolution spectra. From the original catalogue of 268 135 RRLs, we performed a cross-match with the GALAH DR3 main catalogue and found 331 objects in common. However, we must set specific criteria for our study: (1) exposure times for stacked spectra cannot exceed 60 consecutive minutes (3×20 min) because the pulsation cycle of RRLs is shorter than 1 d and we avoid stack spectra collected at very different phases (meaning significantly different atmospheric parameters) and (2) a Signal-to-Noise Ratio (SNR) per pixel of at least 30 (in the red channel, i.e. $\lambda \approx 6500 \text{ \AA}$) is essential for abundance analysis. Applying these criteria, our study focuses on a sub-sample of 78 RRL. Table A1 displays the pulsation properties of our RRL sample. Note that, we provide, for each RRL, both the epoch of maximum light (T_{max}) and the epoch of the mean magnitude on the rising branch T_{ris} . While the former one is the most used in spectroscopic studies and more familiar to the astronomical community, the latter ensures a more precise phasing and is more suited to apply to radial velocity templates (Braga et al. 2021).

We prioritized using light curves from the V band provided by ASAS-SN V and Catalina whenever possible. However, in cases where these were not available for some RR Lyrae stars, we used *Gaia*’s G -band light curves instead. It is important to mention that the amplitude ratio between the G and V bands is nearly 1, according to Clementini et al. (2019). For the RR Lyrae stars whose luminosity amplitudes were used to determine the barycentric radial velocity (RV) with RV templates, we adjusted the amplitudes from the G band to the V band by following the procedure outlined by Clementini et al. (2019).

2.1 Validation of the RRL sample

To determine the characteristics of the RRLs in the GALAH sample, Fig. 1 presents the distribution of the selected RRLs (marked with triangles and circles for RRab and RRc, respectively) in the plane of V -band luminosity amplitude versus pulsation period (known as the Bailey diagram). The symbols within the diagram are colour-coded to reflect the iron abundance, as indicated by the scale on the right side

³<https://gea.esac.esa.int/archive/>

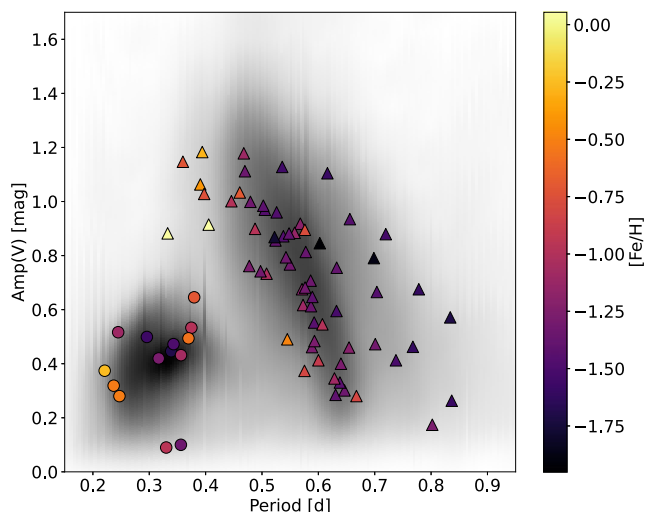


Figure 1. V-band luminosity amplitude versus pulsation period (Bailey Daigram). RRLs in the GALAH’s sample were plotted as triangles (RRab) and circles (RRc). They are colour-coded according to iron abundance (see the scale on the right-hand side). The grey-shaded area shows the distribution of field RRLs included in our photometric catalogue.

of the figure. This serves as a reliable diagnostic for pulsation because it is based on two observables that are unaffected by the uncertainties associated with individual distances and reddening corrections. Data in this panel show that both RRab and RRc variables are located in the regions (grey-shaded areas) typical of Galactic field RRLs. Note that, more metal-rich RRLs are located, as expected, in the short period tail of RRab variables, while the more metal-poor RRLs are in the long period tail (Fiorentino et al. 2015; Fabrizio et al. 2021; Crestani et al. 2021a). The current sample of RRc variables is limited and the trend with metal abundance is less clear.

To enhance our understanding of the pulsation and evolutionary characteristics of our RRLs, the upper section of Fig. 2 displays the chosen RRLs plotted in the colour–colour diagram, specifically in the optical–NIR ($G-H$) versus NIR ($J-K$) plane. The average J , H , K magnitudes were sourced from the 2MASS catalogue. It is important to note that the 2MASS data rely on a limited set of observations, meaning the averages we utilize are derived from these direct measurements rather than being calculated by fitting the individual light curves. We selected this colour–colour plane as chosen for its sensitivity to variations in reddening estimates while remaining unaffected by the uncertainties common to individual distance measurements. The distribution of RRL colours in the GALAH data set shows a strong concordance with that of field RRLs (grey points), as evidenced by their similar colour range and their collective alignment along the reddening vector, indicated by the red arrow. In addition, the RRLs in the GALAH sample were plotted in an optical–NIR CMD to constrain their evolutionary properties. This diagnostic tool is influenced by the uncertainties associated with both reddening and distance calculations. To mitigate the impact of individual reddening variations, their distances were determined using the mid-infrared (MIR) Period–Luminosity–Metallicity (PLZ) relationships for fundamental and first overtone RRLs as given by Neeley et al. (2017). The individual metallicities are the same adopted in the current investigation, while mean $W1$ magnitudes for these stars were obtained from the NEOWISE catalogue (Wright et al. 2010), with their periods and mode classifications sourced from the *Gaia* data base. Dereddening the apparent magnitudes involved using reddening estimates derived from the map provided by Schlafly &

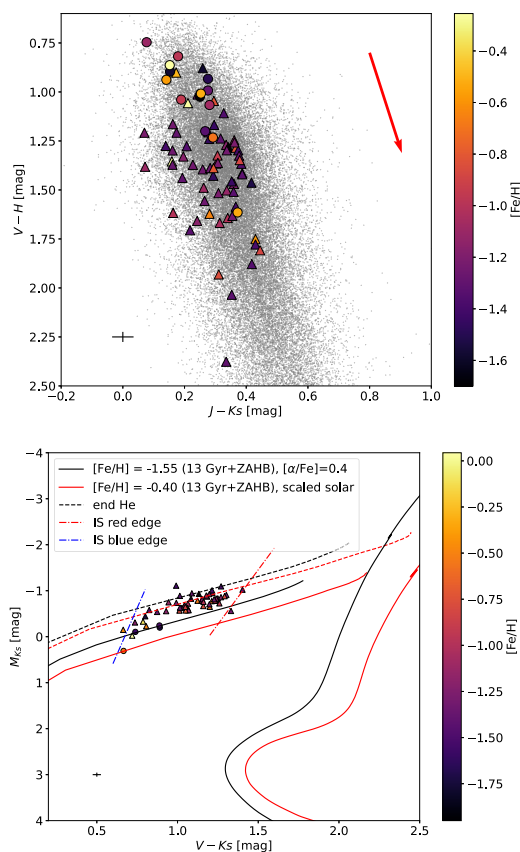


Figure 2. Top: $V-H$ versus $J-K$ colour–colour diagram of the RRLs in the sample (circles). The symbols are colour-coded according to the iron content (see the scale on the right). The grey dots show the distribution of field RRLs included in our photometric catalogue. The red arrow displays the reddening vector. The black cross indicates the average uncertainty on the RRLs of our sample. Bottom: NIR ($V-K$ versus K) Colour–Magnitude Diagram of the RRLs in the GALAH’s sample. The RRL were plotted in this plane by using individual distance determinations and individual reddening estimates (see the text for more details). The black and the red lines display cluster isochrones for $t = 13$ Gyr and different α -enhanced chemical compositions (see labelled values). The horizontal solid lines display the Zero-Age-Horizontal-Branch for the two selected chemical compositions, while the dashed lines indicate the end of core helium burning phases. Symbols are the same as in the top panel. The almost vertical dashed–dotted lines display the hot (blue) and the cool (red) edge of the RRL instability strip (IS) were derived using the pulsation models in Marconi et al. (2015), including metallicities from $Z = 0.0006$ to 0.02. The cross shows the average uncertainties for our RRL sample.

Finkbeiner (2011) and applying the reddening law established by Cardelli, Clayton & Mathis (1989). To enhance the diagnostic’s sensitivity to temperature variations, the RRLs within the GALAH data set were plotted on a $V-K$ versus K CMD, which can be viewed in the lower panel of Fig. 2.

To constrain their evolutionary status we adopted cluster isochrones for $t = 13$ Gyr from the BASTI data set. We selected two α -enhanced chemical compositions (see labelled values) that are representative of the metal-rich tail ($[Fe/H] = -0.40$, red) and of the peak ($[Fe/H] = -1.55$, black) in the metallicity distribution of the GALAH’s sample. Moreover, we also adopted the Zero-Age-Horizontal-Branch (ZAHB, solid lines) and the end of core helium burning (dashed lines).

The ZAHB and the end of core helium burning were selected because theoretical and empirical evidence indicate that the bulk of HB and RRL stars should be distributed within this well-defined magnitude interval. This evidence relies on a solid theoretical prediction: the Asymptotic Giant Branch phase is $\approx 1/2$ orders of magnitude faster than the HB phase. Data plotted in the bottom panel, display, within the errors, a very good agreement with the expected distribution along the HB. Moreover, they display the expected ranking in metal content. Indeed, more metal-rich RRLs are on average fainter than more metal-poor ones. Finally, RRc variables attain $G-K$ colours that are on average systematically bluer than RRab variables (Bono et al. 2011).

3 ABUNDANCE ANALYSIS

Our analysis exploits spectra obtained through the HERMES spectrograph (Sheinis et al. 2015) at the 3.9-meter Anglo-Australian Telescope, located at the Siding Spring Observatory. These spectra are included in the Data Release 3 of the GALAH survey (see De Silva et al. 2015; Buder et al. 2021). HERMES has a nominal spectral resolution $R \approx 28\,000$ in 4 spectral channels: blue (471.5–490.0 nm), green (564.9–587.3 nm), red (647.8–673.7 nm) and infra-red (758.5–788.7 nm). Details on data reduction (including wavelength solution and continuum normalization) can be found in Kos et al. (2017) and Buder et al. (2021). We calculated the radial velocities (RVs) of our sample stars by using only channels blue and green of HERMES spectra because RRLs possess most of the absorption features in the bluest region of the visible bands (their fluxes typically peak at roughly 450 nm). We employed `iSpec` (Blanco-Cuaresma 2019) to conduct cross-correlation with an F-type stellar template and calculate the RVs, as reported in Table A2. The mean difference with GALAH DR3 value is $\Delta(\text{RV}) = -0.17 \pm 0.21 \text{ km s}^{-1}$, which reflects an essentially perfect agreement. Given the distinctive characteristics of RR Lyrae stars, we refrained from adopting the parameters and abundances published in the official GALAH DR3. This decision stems from the fact that the survey (industrial) approach is suboptimal for addressing the unique properties of these warm, variable, and mostly metal-poor stars. A primary issue is the survey’s computation of microturbulence velocities (ξ_t) that are notably low, ranging approximately between $\xi_t \approx 1.2$ and 2 km s^{-1} , and more typical of cool red giant-branch stars. In contrast, RRL stars exhibit microturbulence velocities larger than $2.5\text{--}4 \text{ km s}^{-1}$, as highlighted in studies such as For et al. (2011), Chadid, Sneden & Preston (2017), and Crestani et al. (2021b).

Furthermore, due to the restricted number of spectral lines available, also resulting from gaps between spectral channels, we optimized the effective temperatures (T_{eff}) by fitting the wings of the $H\alpha$ profiles under non-local thermodynamic equilibrium (NLTE) conditions using χ^2 minimization. Emission lines and P Cygni profiles were present in many spectra, causing biased results when fitting effective temperatures. To ameliorate this, we used `KORG` (Wheeler, Casey & Abruzzo 2024; Wheeler et al. 2023) to compute synthetic spectra around the $H\alpha$ line for stars between 5000 and 8000 K, with $\log g$ between 2 and 3, $[\text{Fe}/\text{H}]$ between -2.5 and $+0.5$, and $[\alpha/\text{Fe}]$ between 0 and $+0.4$. With this grid of continuum-normalized fluxes f_λ we defined $\mathbf{X} = 1 - f_\lambda$ to be ‘line absorption’ then used non-negative matrix factorization (Lee & Seung 1999) to approximate the matrix \mathbf{X} by two non-negative matrices \mathbf{W} and \mathbf{H} such that $\mathbf{X} \approx \mathbf{WH}$. We chose to use 24 components for this approximation: \mathbf{H} is a set of 24 non-negative eigenspectra and \mathbf{W} is a set of 24 amplitudes per theoretical spectrum. With the eigenspectra \mathbf{H} , we then constructed a linear model to describe the

stellar flux $y = 1 - \theta\mathbf{H}$, where θ is a set of unknown amplitudes for some observed spectrum. The linearity of this model allows us to add complexity (e.g. emission lines, P Cygni profiles) and ensure that inference remains stable and fast. We added emission and absorption line profiles with unknown parameters that enter multiplicatively to y , and fit these parameters simultaneously with θ , radial velocity v_{rad} , and macroscopic broadening v_{broad} . After fitting, we constructed a mask based on the fitted emission line centroids and standard deviations, and we used this mask to exclude pixels from the subsequent fitting of effective temperature from H_α lines.

To determine T_{eff} values, and for the abundance analysis outlined in this manuscript, we adopted the MARCS stellar grid (1D, plane-parallel models; Gustafsson et al. 2008) and the PYTHON wrapper `TSFitPy` of the `Turbospectrum v.20` (Plez 2012) as described in Gerber et al. (2023). This tool enables the computation of synthetic stellar spectra with NLTE effects for multiple chemical species at once by fitting the normalized synthetic spectra from `Turbospectrum` by χ^2 minimization using the Nelder–Mead algorithm (Gerber et al. 2023). The tool was further optimized and had the addition of some extra features as described in Storm & Bergemann (2023). For this particular project, T_{eff} fitting and ξ_t were added. The latter was done in the following fashion: ξ_t and $[\text{Fe}/\text{H}]$ were fitted using a two-step optimization process to minimize the χ^2 statistic and break the degeneracy between them, as both influence the EW. For each tentative metallicity value, the corresponding optimal ξ_t was identified using the Nelder–Mead algorithm. The final fitted values for both $[\text{Fe}/\text{H}]$ and ξ_t were then obtained by taking their means. An example of the fitting procedure of H_α wings for our sample RRLs is provided in Fig. 3, whereby along with synthetic and observed spectrum we report the best-fitting T_{eff} and the statistical error. The error was calculated based on the χ^2 interval, where the fitted T_{eff} was adjusted until the desired $\Delta\chi^2 = \chi^2 - \chi_{\text{min}}^2 \approx \sigma^2$ was reached.

The optimization of surface gravity ($\log g$) was achieved by leveraging the ionization balance between Fe I and Fe II lines, a practice commonly referenced in literature work. It is important to emphasize that the incorporation of NLTE is pivotal in this context (see e.g. Ruchti et al. 2013). Our method involves fitting all Fe I and Fe II lines within the spectra during each iteration, adjusting the gravity to achieve the least internal scatter. The error on our estimated $\log g$ is then calculated in a similar way as for T_{eff} , that is $\Delta\chi^2 \approx \sigma^2$. Due to the limited presence of ionized iron lines, the internal precision of the surface gravity we derived seldom is less than 0.25 dex. None the less, this limitation does not significantly affect our inferred metallicities and elemental abundances.

We meticulously constructed our line list (reported in Table A5) by choosing notably isolated, unblended, and possibly strong lines that fall within our specified wavelength range and are backed by relatively accurate transition probabilities. We sourced atomic parameters from the *Gaia*–ESO survey (Randich et al. 2022); for a more comprehensive description, readers are directed to Heiter et al. (2021). Our adopted solar abundances are: $A(\text{Fe})_\odot = 7.50$ dex, $A(\text{Ca})_\odot = 6.37$ dex, $A(\text{Si})_\odot = 7.59$ dex, $A(\text{Y})_\odot = 2.21$ dex, $A(\text{Ba})_\odot = 2.18$ dex (see Storm & Bergemann 2023 and references therein).

The uncertainties in our abundance ratios ($[\text{X}/\text{Fe}]$) stem from two main sources: line-by-line scatter, which is represented as error bars in all plots in this paper, and errors associated with stellar parameters. To assess the impact of stellar parameters (i.e. the sensitivities), we altered the T_{eff} , $\log g$, and microturbulence velocity by 100 K, 0.25 dex, and 0.2 km s^{-1} , respectively. After each modification, we reran our analysis to observe the resultant changes in abundance. This

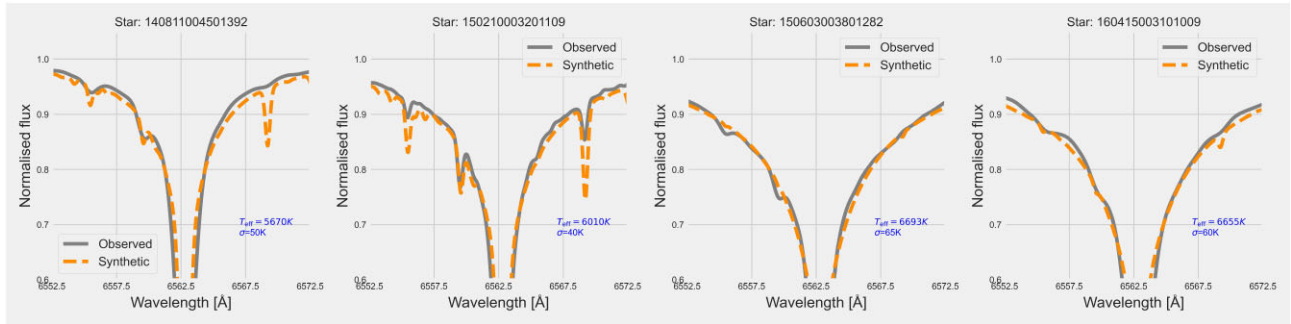


Figure 3. Example of spectral fitting of H α profile in 1D NLTE by TSFitPy.

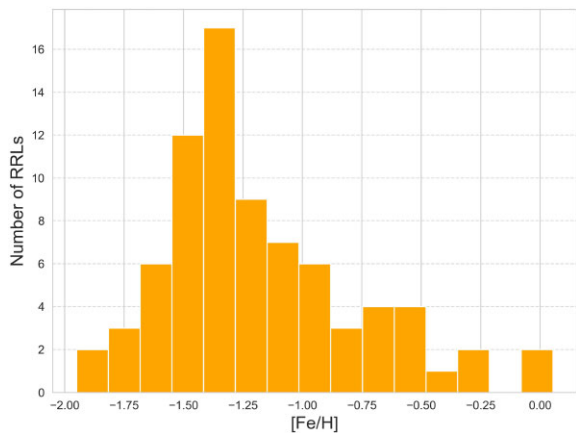


Figure 4. Histogram of [Fe/H] values for the RRL analysed in this work.

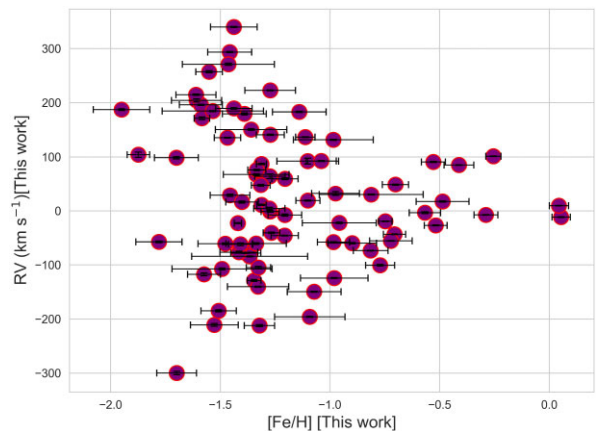


Figure 5. RV values as a function of [Fe/H].

method does not account for the covariance between parameters, meaning it overlooks their interdependence. However, the impact of this covariance is relatively minor, with T_{eff} being the most influential parameter. We calculated errors by considering the internal errors of each parameter and combining them in quadrature. The typical values range between 0.10 and 0.15 dex.

We note that in our work all the published [X/Fe] ratios are calculated adopting an NLTE approach; references for each species are as follows: H (Mashonkina et al. 2008), Mg (Bergemann et al. 2017), Si (Bergemann et al. 2013; Magg et al. 2022), Ca and Fe (Semenova et al. 2020), Y (Storm & Bergemann 2023), and Ba (Gallagher et al. 2020).

4 CHEMISTRY

The metallicity ([Fe/H]) for our sample of RRLs are presented in Fig. 4. The majority of RRLs align with the metallicity distribution function typical of halo stars. This is further supported kinematically, as depicted in Fig. 5. However, the undeniable presence of a metal-rich tail, exhibiting colder disc-like kinematics warrants special attention and is discussed in the subsequent sections of this manuscript.

We have compared our derived parameters, including [Fe/H], with those published in the official GALAH DR3. Notably, the adoption of NLTE in parameter and abundance determination distinguishes GALAH and is absent in surveys like *Gaia*-ESO or APOGEE (e.g. Randich et al. 2022; Abdurro'uf et al. 2022). Consequently, we will confine our comparison for [Fe/H] and atmospheric parameters strictly to GALAH. The difference in T_{eff} values between our estimates and those of GALAH is $\Delta T_{\text{eff}} = -152.7 \pm 16$ K (see

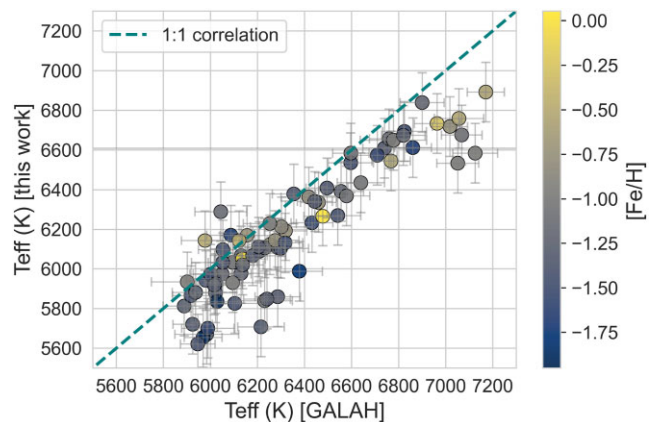


Figure 6. Comparison of this study with T_{eff} estimates from the GALAH DR3.

Fig. 6). This discrepancy can serve as a conservative gauge for the systematic uncertainties influencing our T_{eff} and abundance scale. The higher T_{eff} observed in GALAH can be partially attributed to increased gravities, which were not optimized spectroscopically in the GALAH survey and typically measure +0.4–0.5 dex more than ours. Additionally, as noted earlier, the GALAH survey reports lower ξ , values ranging between 1.5–2 km s $^{-1}$. Cumulatively, these factors lead to a higher metallicity reported by the GALAH survey, being $\Delta[\text{Fe}/\text{H}] = +0.28 \pm 0.02$ dex with respect to our inferred values. The comparison between our estimates and GALAH DR3 metallicity values is reported in Fig. 7.

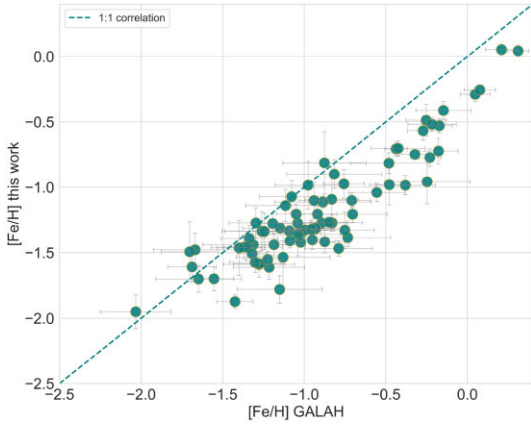


Figure 7. Comparison of our [Fe/H] values with those from the GALAH DR3.

We identified 4 stars in common with the high-resolution spectroscopic analysis by Crestani et al. (2021b), namely CM Ori, V413 CrA, BN Aqr, and AR Oct. Except for CM Ori (for which the Crestani’s [Fe/H] value is -2.05 ± 0.15 to be compared with our -1.46 ± 0.09), the two studies agree fairly well, once observational uncertainties are taken into account: Δ [Fe/H]=+0.11, + 0.14, -0.13 dex, respectively (in the sense ours minus Crestani et al.). To better understand the discrepancies for Cm Ori, we compared our findings with those reported by Crestani et al. (2021). They employed a medium-resolution ($R = 37\,000$) spectrum from the HRS at SALT with a signal-to-noise ratio (SNR) of 38. In contrast, our analysis used a GALAH spectrum with an SNR of 79 in the red band. Both spectra were obtained at a similar phase ($\phi = 0.3$), showing comparable effective temperatures (T_{eff} of 5879 K in our study versus 5820 K by Crestani et al.). However, the difference in $\log g$ values is notable, with our measurement at 2.81 dex compared to 1.22 by Crestani et al. Upon re-analysing the spectrum used by Crestani et al., we determined a T_{eff} of 5860 ± 60 K, $\log g$ of 2.75 ± 0.20 dex, microturbulent velocity (V_t) of 3.00 ± 0.25 km s $^{-1}$, and metallicity ([Fe/H]) of -1.58 ± 0.15 dex. These findings are consistent with our measurements from the GALAH spectrum. It is crucial to highlight that the lower SNR of their spectrum limited the number of Fe I and Fe II lines measured. Additionally, the omission of non-local thermodynamic equilibrium (NLTE) effects in Crestani et al.’s study further amplifies the discrepancies, especially since their gravity measurements do not match photometric values. In our forthcoming paper (Pipwala et al., in preparation), we aim to re-analyse all stars in the Crestani sample using spectral synthesis calculations that include NLTE effects, similar to the methods used in this study.

Our sample star, DT Hya, is analysed in both Marsakov, Gozha & Koval’ (2019) and Preston et al. (2019), with reported [Fe/H] values

of -1.23 and -1.22 , respectively. In comparison, our derived value is $[\text{Fe}/\text{H}] = -1.21 \pm 0.05$. Notably, these estimates are somewhat higher than the -1.43 reported by Chadid et al. 2017, a value that aligns with the earlier result from For et al. (2011). Considering the systematic uncertainties inherent to abundance analysis of warm metal-poor stars, an offset of 0.2 dex can be deemed reasonably acceptable. Stellar parameters and abundances for our 78 RRLs are reported in Table 1, where we list atmospheric parameters, metallicity [Fe/H], [Mg/Fe], [Si/Fe], [Ca/Fe], [Y/Fe], and [Ba/Fe] along with the internal errors as given by the line-by-line scatter.

In Fig. 8, we compare abundance patterns for [Mg/Fe] and [Ca/Fe] for RRLs to stars in the GALAH survey. We adhered to the quality criteria outlined in Buder et al. (2021) and conducted a selective filtering, ensuring that: `flag_sp == 0`, `flag_fe_h == 0`, `flag_alpha_fe == 0`, `snr_c3_irc > 50`, `e_fe_h < 0.10`, and `e_alpha_fe < 0.10`. From an initial catalogue of 588 571 sources, we retained 161 952 stars (28 per cent). In our analysis, the derivation of Mg abundances was limited to a subset of 36 out of 78 stars. This limitation arose from the combination of the intrinsic faintness of the 5711 Å line in the parameter range of our stars (T_{eff} and metallicity) and the relatively low SNR of the spectra. Conversely, Ca abundances were determined for 62 RR Lyrae stars, representing 78 per cent of our sample. Notably, the standard deviation from different lines for [Ca/Fe] ratios was relatively small, typically less than 0.1 dex, leading us to conclude that Ca is the most reliable tracer of α -element abundances for the RR Lyrae stars discussed in this manuscript.

Silicon requires distinct consideration, which is why we have dedicated a separate figure (Fig. 9) to it, distinct from its counterparts Mg and Ca. As extensively discussed by For et al. (2011), the anomalous behaviour of Si abundances in RR Lyrae stars presents a complex challenge. They noted that the NLTE corrections available at the time, as proposed by Shi et al. (2009), were insufficient to fully explain the observed spread. Specifically, their fig. 33 highlights the significant fluctuations in the [Si/Fe] ratios across different pulsational phases for two RR Lyrae stars. Our work includes the more recent NLTE corrections from Bergemann et al. (2013) and Magg et al. (2022). Despite this, we observed considerable internal scatter in the silicon abundances, reaching up to 1 dex for the most extreme cases. Consequently, we opted to retain only those lines yielding silicon abundances within ± 0.2 dex of the [Ca/Fe] values (typically only 1–2 lines per star). We advise readers to interpret silicon data cautiously; it should be seen merely as a supplementary confirmation of the general trends of α -elements with metallicity, rather than as a standalone reliable indicator. For accurate comparisons, modellers should prioritize calcium over silicon when aligning their predictions to RR Lyrae stars, considering calcium as the more reliable tracer.

Fig. 4 demonstrates that the bulk of our RR Lyrae stars is predominantly found in regions of the diagram with [Fe/H] below -1 . These stars are significantly enriched in [Ca/Fe], aligning remarkably

Table 1. Atmospheric parameters and abundances for our sample RR Lyrae stars. This excerpt is for illustrative purposes; the full data set can be accessed online via the CDS.

GALAH _{ID}	T_{eff} (K)	$\log g$ (dex)	ξ_t (km s $^{-1}$)	[Fe/H]	[Mg/Fe]	[Si/Fe]	[Ca/Fe]	[Y/Fe]	[Ba/Fe]
140118002001313	5879 ± 70	2.80 ± 0.20	2.96 ± 0.09	-1.45 ± 0.09	–	–	–	–	-0.35 ± 0.10
140312004501064	6030 ± 50	2.75 ± 0.18	2.77 ± 0.19	-1.18 ± 0.08	0.43 ± 0.10	0.44 ± 0.09	0.30 ± 0.07	–	–
–	–	–	–	–	–	–	–	–	–

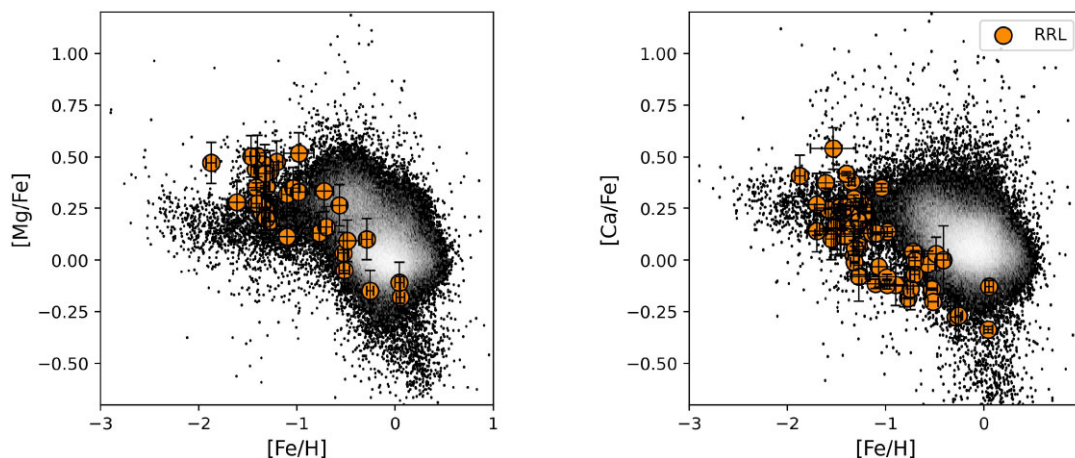


Figure 8. $[X/Fe]$ ratios of α elements Mg, Ca for our RRLs compared to stars in the GALAH survey.

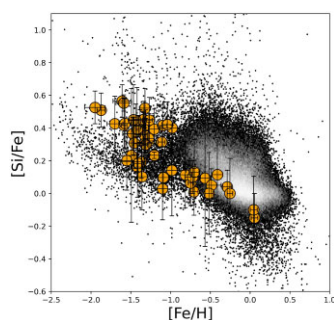


Figure 9. $[Si/Fe]$ ratios for our RRLs compared to stars in the GALAH survey.

well with the distribution patterns of Halo stars as delineated by the GALAH survey. Their chemical content reflects the strong contribution of core-collapse supernovae (CC SNe) in the early evolution of the Milky Way, when nucleosynthesis is dominated by these α -element producers (see e.g. Mashonkina et al. 2019 and references therein).

Intriguingly, at a metallicity around ≈ -1 dex, we observe the emergence of a distinct RRL population, characterized by sub-solar α -element compositions. Here, calcium, benefitting from larger statistical representation and greater measurement precision, serves as a proxy for the trio of α elements. This detection of a metal-rich ($[Fe/H] > -1$) and α -element poor ($[Ca/Fe]$ between ≈ 0 and -0.35) subgroup within RRLs appears to be unique. These stars, exhibiting radial velocities consistent with thin disc kinematics, had been tentatively identified in smaller cohorts by Prudil et al. (2020) and more extensively in larger samples by Crestani et al. (2021b). Our findings corroborate the existence of these ‘anomalous’ RRL stars, a topic currently debated in the field. In a recent study, Iorio & Belokurov (2021) posited a new hypothesis: the presence of young metal-rich RRL stars in the thin disc challenges conventional single-star evolutionary models, which would require implausibly high rates of mass-loss for such metal-rich progenitors. They suggest an alternative scenario in which these stars might be RRL impostors (akin to Binary Evolution Pulsator -BEP), formed through mass transfer in binary systems. However, our results are not in accord with this hypothesis, as binary evolution alone cannot account for the observed low-calcium abundances in these stars. Conversely, these metal-rich RRLs look like a distinct population to the majority of

thin-disc stars. In Fig. 10, we present a comparison of our estimates for $[Mg/Fe]$ and $[Ca/Fe]$ with the findings from Crestani et al. (2021b) high-resolution study. It is important to note that Crestani et al. did not adjust their results for NLTE effects. Despite this, there is a general agreement in the trends observed within the RRL population. However, Crestani et al. data show notably more scatter in Mg, particularly for metallicities lower than $[Fe/H] = -1.5$. The cause of this increased scatter, whether it is an inherent feature or a result of methodological choices such as omitting NLTE corrections, will be the subject of future research.

To further explore this metal-rich population, we determined the abundance of neutron-capture elements, specifically yttrium and barium. Elements heavier than iron are produced via neutron-capture processes: slow (s-process) and rapid (r-process). The dominant mechanism for r-process production, involving neutron star mergers, neutron-star-black hole mergers, and events like hypernovae, collapsars, and magnetorotational supernovae, remains debated (Cowan et al. 2021; Chen et al. 2024). The s-process occurs mainly in asymptotic giant branch (AGB) stars, synthesizing elements from strontium to lead through the $^{13}C(\alpha,n)^{16}O$ reaction (Karakas & Lattanzio 2014), and in massive and low-metallicity, fast-rotating stars for elements (Pignatari et al. 2010; Choplin et al. 2018; Limongi & Chieffi 2018). In these environments, neutron source reactions primarily involve $^{22}Ne(\alpha,n)^{25}Mg$ (see Lugaro et al. 2023 and references therein). Studies confirm the s-process as the main source of yttrium and barium in the Solar System, contributing 76 and 78 percent to their formation, respectively, with the r-process accounting for the remainder (Busso et al. 2021). Therefore, these elements are commonly classified as s-process elements, although it is important to note that several of the odd Ba isotopes are also produced via the r-process. Importantly, at metallicity lower than solar, the contribution of the s-process and r-process to the production of Y and Ba might differ. For these elements, when the $[Fe/H]$ is less than ≈ -2 , their formation is primarily ascribed to the r-process (see e.g. Tolstoy, Battaglia & Cole 2008; Reichert et al. 2020, and references therein), given that low-mass AGB stars evolve on longer time-scales (\approx Gyrs).

We derived $[Y/Fe]$ ratios for 52 stars and $[Ba/Fe]$ ratios for 63 stars, with 43 RRLs having measurements for both elements. The 1:1 correlation between $[Ba/H]$ and $[Y/H]$, as shown in Fig. 11, lends strong credibility to our determined values. In Fig. 12, we present the trends of $[Y/Fe]$ and $[Ba/Fe]$ with metallicity, comparing our results with those from Bensby, Feltzing & Oey (2014). We

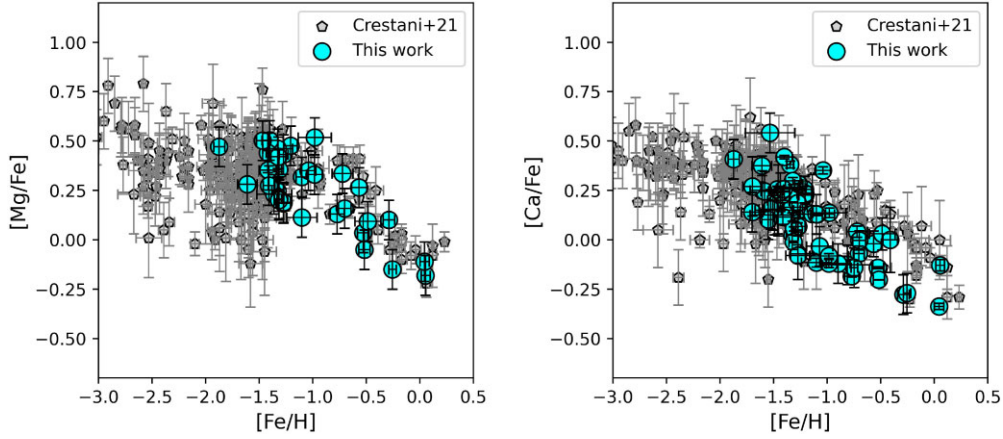


Figure 10. Comparison of RRL in the present study with those analysed by Crestani et al. (2021b).

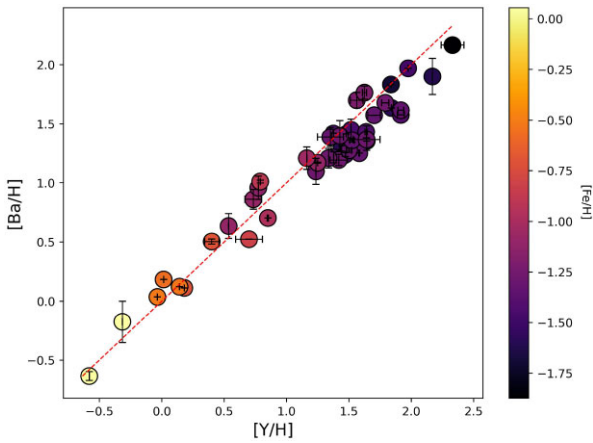


Figure 11. Run of [Ba/H] with [Y/H] and the 1:1 correlation for our sample RRLs.

chose not to compare with GALAH DR3 due to the considerable scatter observed in these heavy-element abundances at each given metallicity bin. However, it is important to note that the Bensby et al.’s abundances were not corrected for NLTE effects; despite this, the overall trend should remain credible (corrections for Y II and Ba II

lines should remain within ≈ 0.2 dex). Our RRL sample exhibits a notable spread in Y or Ba abundances for metallicity below $[\text{Fe}/\text{H}] \lesssim -1$. Our study indicates that metal-rich RRL stars significantly differ from the typical thick/thin disc population, particularly in their lower levels of s-process elements.

In a comprehensive study of 380 stars across 13 dwarf spheroidal and ultra-faint galaxies, Reichert et al. (2020) analysed the abundance of n-capture elements. Their work revealed that the emergence of the s-process (as indicated in the $[\text{Eu}/\text{Ba}]$ versus $[\text{Ba}/\text{H}]$ diagram, refer to their Fig. 16) appears to start at higher metallicities in galaxies with greater stellar mass. Regardless of this overall pattern, there is significant variation in the levels of Ba and Y at any given metallicity. From Fig. 13, we observe that at higher metallicities ($[\text{Fe}/\text{H}] \gtrsim -1$), the Ba abundance patterns in the Fornax and Sgr galaxies differ somewhat from those in our RRLs, despite considerable scatter. Conversely, the $[\text{Y}/\text{Fe}]$ ratios in metal-rich RRLs are comparable to those in Fornax and Sgr galaxies. While our RRLs show solar or sub-solar $[\text{X}/\text{Fe}]$ ratios for Y and Ba (with $[\text{heavy s-process}/\text{light s-process, hs/ls}] \approx 0$), stars in Fornax and Sagittarius exhibit lower Y abundances relative to Ba. This pattern, where the second-peak element Ba is enhanced over the first-peak Y (i.e. a higher $[\text{hs/ls}]$ ratio), suggests a significant contribution from low-metallicity AGBs. Minelli et al. (2021) conducted a comprehensive chemical analysis of 30 giant stars in the Large Magellanic Cloud (LMC), 14 in the Sagittarius dwarf

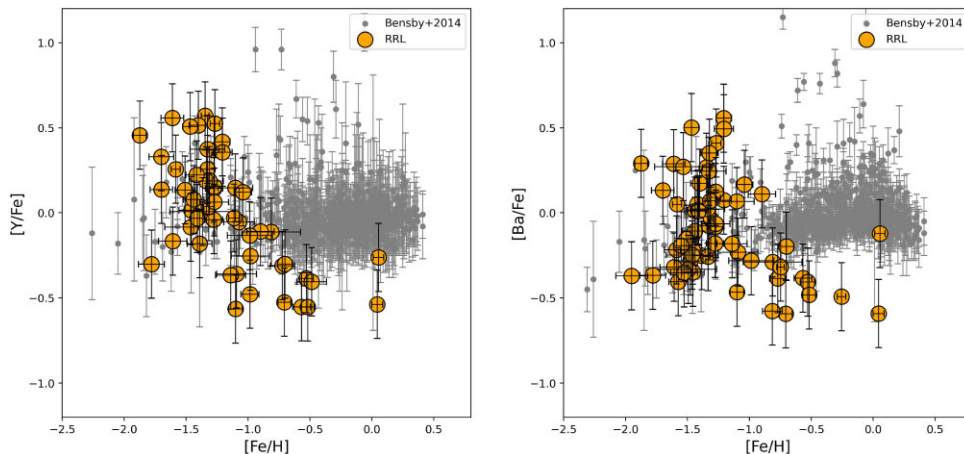


Figure 12. $[\text{X}/\text{Fe}]$ ratios of n-capture elements Y, Ba for our RRLs compared to abundances in disc and halo stars by Bensby et al. (2014).

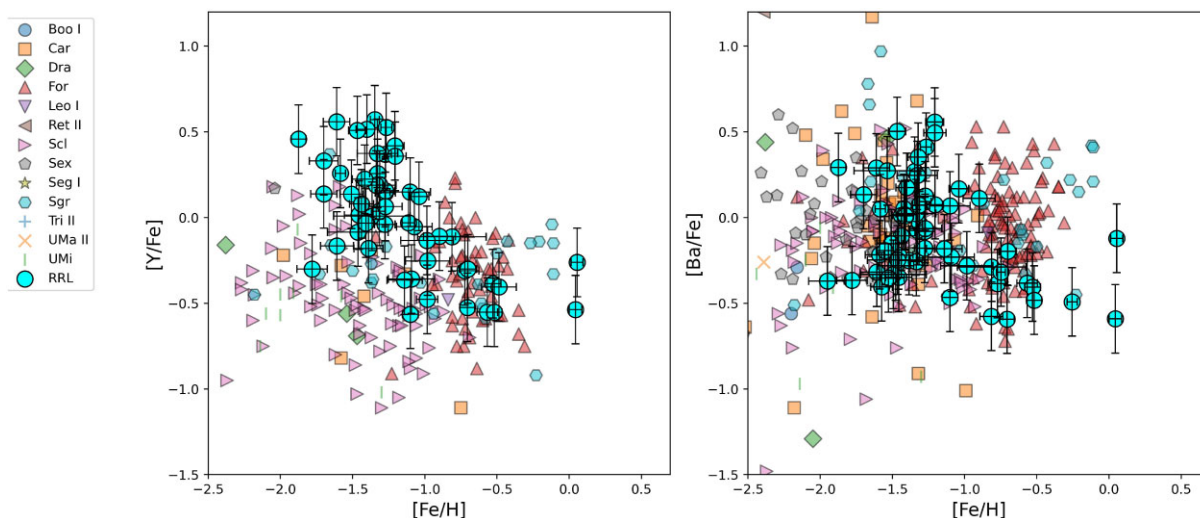


Figure 13. $[X/Fe]$ ratios of n -capture elements Y, Ba for our RRLs compared to abundances in the sample of dSph stars by Reichert et al. (2020).

galaxy, and 14 in the Milky Way. This study was based on high-resolution spectra obtained using the UVES–FLAMES spectrograph and aimed to homogeneously compare abundance patterns in the three different galaxies. The study identified a notable variation in Y abundances in stars from both Sgr and the Large LMC, with the latter exhibiting lower Y levels, similar to the findings in our metal-rich RR Lyrae stars. Contrarily, Zr does not show a deficiency, while barium is found to be significantly abundant. This results in a high $[hs/ls]$ ratio, particularly in stars with a metallicity above -0.5 . The study suggests two potential explanations for this trend of increasing $[hs/ls]$ with metallicity: either the presence of comparatively metal-poor AGB stars in the LMC and Sagittarius relative to the Milky Way, or a reduced contribution from the most massive stars (see Minelli et al. 2021 for details). Interestingly, considering all literature studies from 1995–2017, Gozha, Marsakov & Koval (2021) found that Y abundances in metal-rich RRLs are significantly sub-solar and different from Galactic stars, in line with our findings. In a recent publication, Mucciarelli et al. (2023a) reported higher levels of s-process elements like Zr, Ba, and La in the Small Magellanic Cloud (SMC) compared to the Milky Way. A subsequent study by the same team (Mucciarelli et al. 2023b) analysed the metallicities and s-process elements in three SMC globular clusters: NGC 121 ($[Fe/H] = -1.18$), NGC 339 ($[Fe/H] = -1.24$), and NGC 419 ($[Fe/H] = -0.58$), revealing varied patterns of s-process elements. NGC 121 and NGC 339 showed sub- and super-solar $[Y/Fe]$ and $[Ba/Fe]$ ratios, respectively, while NGC 419, the youngest and most metal-rich, exhibited a mix of ratios, suggesting a potential influence of low-metallicity AGB stars in its chemical evolution. This highlights the distinct chemical characteristics of the SMC’s stellar populations with respect to our RRLs. Feuillet et al. (2022) analysed APOGEE DR17 data and identified an ancient, metal-rich, accreted component within the ‘cool’ Galactic disc of the Milky Way. Alongside red giant stars, they also pinpointed a small group of RR Lyrae variables with disc kinematics that exhibit the same chemical signature as the accreted red giant stars found in the disc. In their study, they identified key indicators for differentiating accreted and *in situ* stars, specifically focusing on aluminium ($[Al/Fe]$) and the $[Mn/Mg]$ ratio (as illustrated in their fig. 1). For our sample stars, we could not analyse Al and Mn due to limitations of low signal-to-noise ratios and insufficient spectral coverage/resolution (and Mg was inferred only for a small sub-sample because of the weakness of the 5711 Å

line at the temperature/metallicity of our RRLs). None the less, we examined the trend of cerium, the only s-process element available in APOGEE data. Regrettably, the data on cerium abundance in the accreted red giant population varied widely, showing a mix of both low- and high-cerium levels, which made it challenging to reach conclusive findings.

5 DYNAMICS

We explore the dynamical properties of these stars by characterizing their orbits. To integrate the orbits we use the code AGAMA (Vasiliev 2019), and adopted the potential of the Galaxy by McMillan (2017). We assume the same position of the Sun in the Galaxy adopted by Ceccarelli et al. (2024): height of the Sun above the Galactic plane $z_{\odot} = 20.8$ pc (Bennett & Bovy 2019), distance of the Sun from the Galactic centre $R_{\odot} = 8.122$ kpc (GRAVITY Collaboration et al. 2018). The solar velocity has been obtained by combining the definition of the local standard of rest by Schönrich, Binney & Dehnen (2010) with the proper motion of Sgr A* from Reid & Brunthaler (2004). In this frame, the 3D components of the Sun’s velocity are $(U_{\odot}, V_{\odot}, W_{\odot}) = (12.9, 245.6, 7.78)$ km s $^{-1}$ (Drimmel & Poggio 2018). We integrate the orbits for 3 Gyr, starting from the current position and velocity of the stars. To estimate the uncertainty of the orbital parameters, for each star, we run 100 Monte Carlo simulations of the orbit, by assuming Gaussian errors in distance, proper motion and radial velocity. The final values of the orbital parameters are given by the median of the distributions, whereas the associated uncertainties correspond to their 16th and 84th percentiles.

This allows us to gather information on the areas of the Galaxy where these stars move. In particular, we compute the circularity of the orbit (see e.g. Massari, Koppelman & Helmi 2019a), defined as the angular momentum J_z along the vertical z -axis, normalized by the angular momentum of a circular orbit with the same binding energy E :

$$\lambda_z = \frac{J_z}{J_{\max}(E)}. \quad (1)$$

Following Zhu et al. (2018) and Santucci et al. (2023), we separate orbits into four different components: a cold component with near circular orbits (representing the thin disc), a warm component in between (representing the thick disc), a hot component with near

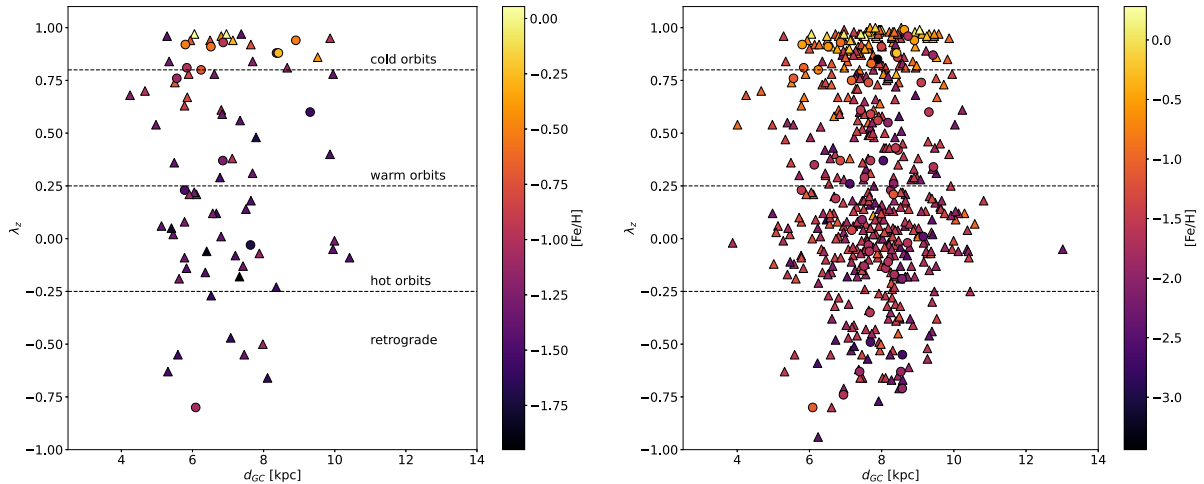


Figure 14. Left-hand panel: The circularity λ_z of the orbits in our GALAH sample as a function of the Galactocentric distance (d_{GC}). Filled circles display the position of RRab variables, while the triangles are R Rc variables. The symbols are colour-coded according to the iron abundance (see the colour bar on the right). Horizontal lines divide the sample into the various Galactic components introduced in Section 5. Right-hand panel: Circularity of the orbits but for the full sample of 535 RRLs.

radial orbits (representing the halo and/or the bulge), and a retrograde component. We assign stars to each of these components according to their orbit circularity λ_z : cold orbits are characterized by $\lambda_z > 0.8$, warm orbits by $0.25 < \lambda_z \leq 0.8$, hot orbits by $-0.25 < \lambda_z \leq 0.25$, and retrograde orbits by $\lambda_z \leq -0.25$. Implications of the dynamical properties of our sample RRLs are discussed in the next Section.

6 DISCUSSION

The left-hand panel of Fig. 14 shows the circularity computed for the orbits of the RRLs in the GALAH sample, as a function of their Galactocentric distance (d_{GC}). The horizontal lines separate the orbits in four kinematic bins and the symbols are colour-coded according to their iron abundance (see colour bar on the right). Average chemical properties for RRLs in each kinematic bin are reported in Table A4. We discuss in the following several compelling features that warrant a closer examination and discussion.

Retrograde RRLs – We discovered seven out of the 78 RRLs to display retrograde orbits. The key pulsation parameters and chemical abundances are listed in Table 2. Among these, two exhibit metallicities around $[\text{Fe}/\text{H}] \approx -1$ and have $[\text{Ca}/\text{Fe}]$ ratios similar to the Sun or slightly lower. The other five stars align closely with typical halo star characteristics, showing low metallicity and enhanced α -elements. The neutron-capture elements yttrium and barium in these stars are nearly solar or just below, which does not significantly deviate from the general distribution. However, the large scatter in metallicity below -1 for Y and Ba adds complexity to understanding the patterns of these heavy elements. We cannot conclusively determine whether these stars originated outside our Galaxy, even though their dynamical properties strongly support this interpretation. Interestingly, two of the metal-poor retrograde RR Lyrae stars, *Gaia* DR3 3 892 831 505 236 595 456 and 4737956618117144832, appear to be connected to the *Gaia*-Sausage-Enceladus structure, based on a match with the catalogue by Helmi et al. (2018).

Metal-rich RRLs – The bulk of metal-rich RRLs are characterized by cold orbits. Data plotted in the left-hand panel in Fig. 14 shows that almost one-third (23/78) of the sample stars has a λ_z larger than ~ 0.8 .

This preliminary evidence indicates that metal-rich RRLs are far from being rare objects. Their origin should follow an evolutionary channel similar to the RRLs in the metal-intermediate and the metal-poor regime (Bono et al. 1997; Marconi et al. 2018). The absence of these objects in prior spectroscopic (Preston 1959; Walker & Terndrup 1991; Sneden et al. 2018) and photometric (Pietrukowicz et al. 2020; Mullen et al. 2021, 2022) studies primarily stems from an observational bias. These investigations were predominantly focused on the Galactic halo, leading to a preference for detecting objects within that region. The present sample, while still confined to a narrow range of Galactocentric distances, includes disc RRLs, thereby providing a broader and more representative sample of the metallicity distribution extremes. Moreover, there is mounting evidence that metal-rich RRLs are also α -poor. This evidence was originally brought forward by Magurno et al. (2018, 2019) using a mix of high-resolution spectra for cluster RRLs and similar measurements for field RRLs available in the literature. A similar conclusion was also reached by Marsakov, Gozha & Koval (2018) by collecting measurements available in the literature. However, solid constraints on the α -element abundance of metal-rich RRLs were only reached with the homogeneous and detailed spectroscopic investigations by Crestani et al. (2021a, b) based on high-resolution spectra in which metal-rich RRLs approach solar α abundances and in the very metal-rich regime they exhibit sub-solar α -elements ratios ($[\alpha/\text{Fe}] < 0$). Arguments grounded in physical principles, including kinematic evidence from cold orbits, iron content consistent with solar iron abundance as reported by Fabrizio et al. (2021), and the ratios of α -element to iron abundances ($[\alpha/\text{Fe}] \approx 0$, as shown in Figs 7, 8, and 9), compellingly indicate that metal-rich RR Lyrae stars share characteristics akin to those of a disc population. None the less, when comparing metal-rich RRLs with non-variable disc stars at similar metallicity levels, we find that RRLs have slightly lower abundances of α -elements. Further, based the abundance of the two *s*-process elements Y and Ba are systematically lower than in typical disc stars at the same iron abundance. This pattern implies that metal-rich RRLs might not be a conventional ‘disc population’. Instead, they could represent either a ‘drifting disc population’ or an ‘ancient native disc population’. The nature of the ‘drifting disc

Table 2. Properties of the retrograde RRLs.

RRL	P (d)	Amp (mag)	[Fe/H]	[Ca/Fe]	[Y/Fe]	[Ba/Fe]
<i>Gaia</i> DR3 294 072 906 063 827 072	0.390 316	0.389	-1.90 ± 0.20	–	–	–
<i>Gaia</i> DR3 315 028 326 379 733 760	0.563 123	1.123	-1.61 ± 0.20	0.28 ± 0.20	–	–
<i>Gaia</i> DR3 593 827 920 716 707 584	0.548512	0.869	-1.59 ± 0.20	–	–	–
<i>Gaia</i> DR3 837 077 516 695 165 824	0.349 358	0.493	–	–	–	–
<i>Gaia</i> DR3 1 058 066 262 817 534 336	0.660 399	0.896	-1.83 ± 0.03	0.40 ± 0.20	–	–
<i>Gaia</i> DR3 1 167 409 941 124 817 664	0.340 828	0.387	-1.88 ± 0.11	0.44 ± 0.07	–	–
<i>Gaia</i> DR3 1 252 055 779 366 233 344	0.609 085	0.905	-1.53 ± 0.20	–	–	–
<i>Gaia</i> DR3 1 356 103 870 372 434 560	0.630 352	0.955	-2.01 ± 0.20	–	–	–
<i>Gaia</i> DR3 1 398 766 021 041 835 648	0.469 997	0.847	-1.64 ± 0.30	–	–	–
<i>Gaia</i> DR3 1 461 194 435 841 276 288	0.648 538	0.305	-1.27 ± 0.03	–	–	–
<i>Gaia</i> DR3 1 518 851 996 671 918 208	0.558 627	1.047	-1.06 ± 0.19	–	–	–
<i>Gaia</i> DR3 1 519 628 565 414 140 160	0.668 139	0.717	-2.59 ± 0.28	–	–	–
<i>Gaia</i> DR3 1 786 827 307 055 763 968	0.547 243	0.935	-1.55 ± 0.08	0.40 ± 0.06	–	–
<i>Gaia</i> DR3 2 022 835 523 801 236 864	0.594 130	0.960	-1.58 ± 0.20	–	–	–
<i>Gaia</i> DR3 2 150 632 997 196 029 824	0.602 674	1.194	-1.70 ± 0.20	0.23 ± 0.20	–	–
<i>Gaia</i> DR3 2 309 225 008 197 193 856	0.784 905	0.627	-2.31 ± 0.20	–	–	–
<i>Gaia</i> DR3 2 622 375 506 154 471 680	0.469 679	1.112	-1.35 ± 0.03	0.38 ± 0.02	0.57 ± 0.02	0.27 ± 0.10
<i>Gaia</i> DR3 2 737 233 514 449 351 680	0.496 716	1.219	-1.43 ± 0.19	–	–	–
<i>Gaia</i> DR3 2 808 687 029 926 911 360	0.554 537	0.880	-1.38 ± 0.19	–	–	–
<i>Gaia</i> DR3 2 817 589 255 885 467 520	0.607 354	1.239	-1.41 ± 0.19	–	–	–
<i>Gaia</i> DR3 2 852 346 261 548 304 896	0.306 493	0.449	-1.94 ± 0.19	–	–	–
<i>Gaia</i> DR3 2 853 512 332 285 518 592	0.566 067	0.795	-1.76 ± 0.19	–	–	–
<i>Gaia</i> DR3 2 973 463 347 160 718 976	0.581 474	1.005	-1.88 ± 0.28	0.39 ± 0.27	–	–
<i>Gaia</i> DR3 3 471 095 334 863 875 456	0.778 211	0.675	-1.61 ± 0.09	0.37 ± 0.05	0.56 ± 0.10	0.29 ± 0.15
<i>Gaia</i> DR3 3 486 473 757 325 180 032	0.650 309	0.467	-2.54 ± 0.08	–	–	–
<i>Gaia</i> DR3 3 632 110 703 852 863 616	0.651 558	0.984	-2.46 ± 0.31	–	–	–
<i>Gaia</i> DR3 3 677 686 044 939 929 728	0.525 756	0.938	-1.88 ± 0.00	0.34 ± 0.07	–	–
<i>Gaia</i> DR3 3 765 574 712 337 027 456	0.537727	0.802	-1.49 ± 0.03	0.30 ± 0.06	–	–
<i>Gaia</i> DR3 3 892 831 505 236 595 456	0.767 711	0.462	-1.61 ± 0.11	0.25 ± 0.10	-0.17 ± 0.10	-0.32 ± 0.02
<i>Gaia</i> DR3 3 915 944 064 285 661 312	0.598 638	1.040	-1.52 ± 0.20	–	–	–
<i>Gaia</i> DR3 3 917 248 286 939 430 144	0.726 806	0.524	-2.36 ± 0.20	–	–	–
<i>Gaia</i> DR3 4 179 431 168 210 587 648	0.356 331	0.432	-1.07 ± 0.12	-0.03 ± 0.10	-0.05 ± 0.05	–
<i>Gaia</i> DR3 4 487 364 105 534 330 112	0.603 347	0.910	-1.58 ± 0.19	–	–	–
<i>Gaia</i> DR3 4 624 119 506 369 712 384	0.583 342	0.876	-2.57 ± 0.20	–	–	–
<i>Gaia</i> DR3 4 631 934 555 845 355 136	0.555 815	0.692	-2.07 ± 0.20	–	–	–
<i>Gaia</i> DR3 4 643 606 391 466 365 824	0.675 377	0.854	-1.72 ± 0.20	–	–	–
<i>Gaia</i> DR3 4 685 757 887 726 594 816	0.732 911	0.515	-2.70 ± 0.20	–	–	–
<i>Gaia</i> DR3 4 692 528 057 537 147 136	0.405 791	0.422	-1.60 ± 0.20	–	–	–
<i>Gaia</i> DR3 4 737 725 170 919 494 912	0.662 187	0.617	-2.39 ± 0.20	–	–	–
<i>Gaia</i> DR3 4 737 956 618 117 144 832	0.572 856	0.617	-1.10 ± 0.14	-0.12 ± 0.02	0.15 ± 0.10	0.07 ± 0.00
<i>Gaia</i> DR3 4 760 456 779 256 739 968	0.649 671	0.387	-1.87 ± 0.20	–	–	–
<i>Gaia</i> DR3 4 788 620 567 737 382 144	0.613 053	0.500	-1.50 ± 0.20	–	–	–
<i>Gaia</i> DR3 4 818 854 972 838 127 360	0.478 862	0.795	-1.22 ± 0.03	0.30 ± 0.06	–	–
<i>Gaia</i> DR3 4 854 350 575 436 127 488	0.729 404	0.724	-2.06 ± 0.20	–	–	–
<i>Gaia</i> DR3 5 011 834 347 435 737 344	0.637 068	0.763	-2.33 ± 0.20	–	–	–
<i>Gaia</i> DR3 5 094 203 642 556 959 744	0.608 816	0.945	-2.42 ± 0.20	–	–	–
<i>Gaia</i> DR3 5 281 881 584 407 284 352	0.572 398	0.862	-1.51 ± 0.20	–	–	–
<i>Gaia</i> DR3 5 555 745 531 172 521 344	0.797 322	0.171	-2.24 ± 0.20	–	–	–
<i>Gaia</i> DR3 5 638 928 606 644 888 448	0.552 546	0.590	-1.57 ± 0.20	–	–	–
<i>Gaia</i> DR3 5 696 434 679 682 159 872	0.285 668	0.220	-2.67 ± 0.15	0.37 ± 0.20	–	–
<i>Gaia</i> DR3 5 743 059 538 967 112 576	0.537 228	0.751	-2.17 ± 0.03	0.35 ± 0.06	–	–
<i>Gaia</i> DR3 5 909 759 314 361 595 520	0.710 373	0.801	-2.39 ± 0.20	–	–	–
<i>Gaia</i> DR3 6 120 897 123 486 850 944	0.493 990	0.789	-1.53 ± 0.03	0.20 ± 0.06	–	–
<i>Gaia</i> DR3 6 341 917 480 568 293 120	0.457 998	0.825	-1.66 ± 0.20	–	–	–
<i>Gaia</i> DR3 6 345 324 587 928 571 648	0.621 858	0.899	-1.66 ± 0.20	–	–	–
<i>Gaia</i> DR3 6 380 659 528 686 603 008	0.550 081	0.995	-1.86 ± 0.01	0.31 ± 0.01	–	–
<i>Gaia</i> DR3 6 428 374 141 448 297 856	0.527 141	1.050	-1.53 ± 0.20	–	–	–
<i>Gaia</i> DR3 6 434 640 155 133 754 368	0.719 611	0.879	-1.53 ± 0.23	0.54 ± 0.10	–	0.27 ± 0.10
<i>Gaia</i> DR3 6 502 711 401 043 594 496	0.508 403	1.004	-1.99 ± 0.20	–	–	–
<i>Gaia</i> DR3 6 519 995 861 275 291 008	0.550 309	0.928	-2.07 ± 0.20	–	–	–
<i>Gaia</i> DR3 6 541 769 554 459 131 648	0.281 110	0.238	-1.66 ± 0.09	0.39 ± 0.20	–	–
<i>Gaia</i> DR3 6 625 215 584 995 450 624	0.546 740	1.048	-1.61 ± 0.18	0.39 ± 0.13	–	–
<i>Gaia</i> DR3 6 662 886 605 712 648 832	0.316 907	0.436	-2.60 ± 0.18	0.05 ± 0.19	–	–

Table 2 – *continued*

RRL	P (d)	Amp (mag)	[Fe/H]	[Ca/Fe]	[Y/Fe]	[Ba/Fe]
<i>Gaia</i> DR3 6 673 750 914 465 028 096	0.683 173	0.793	-2.45 ± 0.20	–	–	–
<i>Gaia</i> DR3 6 749 657 142 798 141 184	0.639 409	0.718	-2.60 ± 0.20	–	–	–
<i>Gaia</i> DR3 6 795 546 531 894 178 816	0.632 184	0.595	-1.53 ± 0.11	0.15 ± 0.10	–	-0.35 ± 0.10
<i>Gaia</i> DR3 6 796 320 308 904 070 016	0.544 448	0.986	-1.49 ± 0.04	0.31 ± 0.04	–	–
<i>Gaia</i> DR3 6 883 653 108 749 373 568	0.447 745	1.090	-1.45 ± 0.16	0.10 ± 0.14	–	–

population’ is currently unclear, being debated as either a purely accreted component, termed ‘aliens’ by Zinn et al. (2020), or as ‘commuters’ as identified by Snaith et al. (2016) and Monachesi et al. (2019). These commuters are objects formed *in situ* within the Milky Way’s virial radius but from gas imported by a massive satellite.

Metal-intermediate RRLs – RRLs characterized by warm orbits roughly include 36 per cent of the sample (28/78) and display smooth transition when moving from RRLs with hot and cold orbits.

Metal-poor RRLs – RRLs with hot orbits are characterized by metal-poor iron abundances. The iron abundances of the retrograde component are very similar to the RRLs with hot orbits; although, they are considered a typical accreted component their metallicity distribution is similar to Halo RRLs.

We should note that our sample size is somewhat restricted, limiting our ability to draw definitive conclusions about the evolutionary, pulsation, and kinematic properties of field RRLs. Thus, we have chosen to utilize the RRL sample for which previously determined iron and α -element abundances are reliable. These determinations were made using high-resolution, high signal-to-noise ratio spectra and LTE approximations (Magurno et al. 2019; Crestani et al. 2021a, b).

Additionally, we incorporated RRLs with consistent iron abundances and radial velocity (RV) data sourced from existing studies (Zinn et al. 2020). This resulted in a spectroscopic catalog of 535 RRLs. The right-hand panel of Fig. 14 illustrates the circularity of the complete RRL sample in relation to their distance from the Galactic centre. The observations presented in this figure corroborate the findings derived from the GALAH sample. Key observations are elaborated on below:

Retrograde RRLs – The sample size of field RRLs with retrograde orbits is still of the order of 8 per cent (44/535) and their iron abundance is either metal-poor or metal-intermediate (below ≈ -1)

Metal-rich RRLs – The metal-rich RRLs include a significant fraction (17 per cent more metal-rich than -1 dex) of the entire RRL sample. The sharp edge for Galactocentric distance smaller than 5 kpc and larger than 11 kpc is a consequence of the biases associated with the limiting magnitude and the large extinction close to the Galactic plane.

Fig. 15 shows the distribution of the orbit circularity for the entire RRL sample. The red and the blue hatched areas display the orbit circularities based on high-resolution (HR) spectra and on the entire (HR + LR [low resolution]) spectroscopic sample. The blue solid line shows the smoothed distribution estimated by using a Gaussian kernel with unitary weight and σ equal to the error of the individual estimates. The vertical dashed lines display the four kinematics groups defined in Fig. 14. Data plotted in this figure display two well-defined peaks associated with RRLs with hot ($-0.25 < \lambda_z \leq 0.25$) and cold ($\lambda_z > 0.8$) orbits. The current findings suggest that the latter sample is one of the main components of field RRLs and not a minority group. This implies a similar evolutionary channel. Moreover, the transition from disc-like to halo/bulge-like

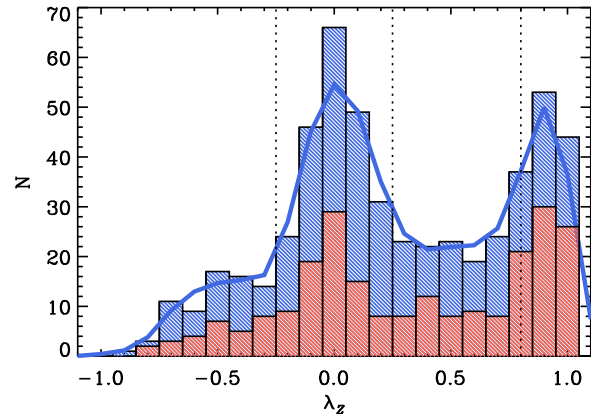


Figure 15. Orbit circularity (λ_z) distribution for the entire RRL sample. The red hatched area shows RRLs with iron abundances based on HR spectra, while the blue hatched area the cumulative iron distribution function (HR + LR). The blue solid line displays the running average over the entire sample, while the vertical dashed lines are the boundaries of the four kinematic groups.

RRLs seems to be quite smooth with a well-defined minimum for $\lambda_z \sim 0.5$. These are the typical orbit circularities of thick disc stars. Note that, the current data seem to indicate a smooth transition between thin and thick disc RRLs, thus suggesting that two different disc components formed at similar ages. This finding fully supports the results obtained by Beraldo e Silva et al. (2021), and more recently by Wu et al. (2023) using main-sequence turn off field stars. Finally, let us mention that RRLs with retrograde orbits appear to be an addendum to the long tail of the RRLs with hot orbits. Indeed the smoothed distribution shows a sharp change in the slope for λ_z between ~ -0.25 and -0.30 .

To investigate on a more quantitative basis, the difference in metallicity distribution among the four different kinematic bins, the left panels of Fig. 16 show the iron distribution function based on HR spectra (red hatched area) and entire (HR + LR) spectroscopic sample (blue hatched area). The blue solid line shows the smoothed iron distribution function. The latter was smoothed using a Gaussian kernel with unitary weight and σ equal to the error of the individual estimates. The mean and standard deviation of the smoothed distributions are also labelled. The iron distribution functions plotted in the left panels show that the main peaks agree, within the errors, with the peak in iron abundance for field RRLs found by Fabrizio et al. (2021) ($[\text{Fe}/\text{H}] = -1.26$, $\sigma = 0.60$ (535 stars) versus $[\text{Fe}/\text{H}] = -1.51$, $\sigma = 0.41$ (9015 stars) using the largest sample of LR spectra and the ΔS method.

The key difference in the iron distribution function is that the spread of iron abundance for RRLs with cold orbits is systematically larger than for the other kinematic bins. This subsample

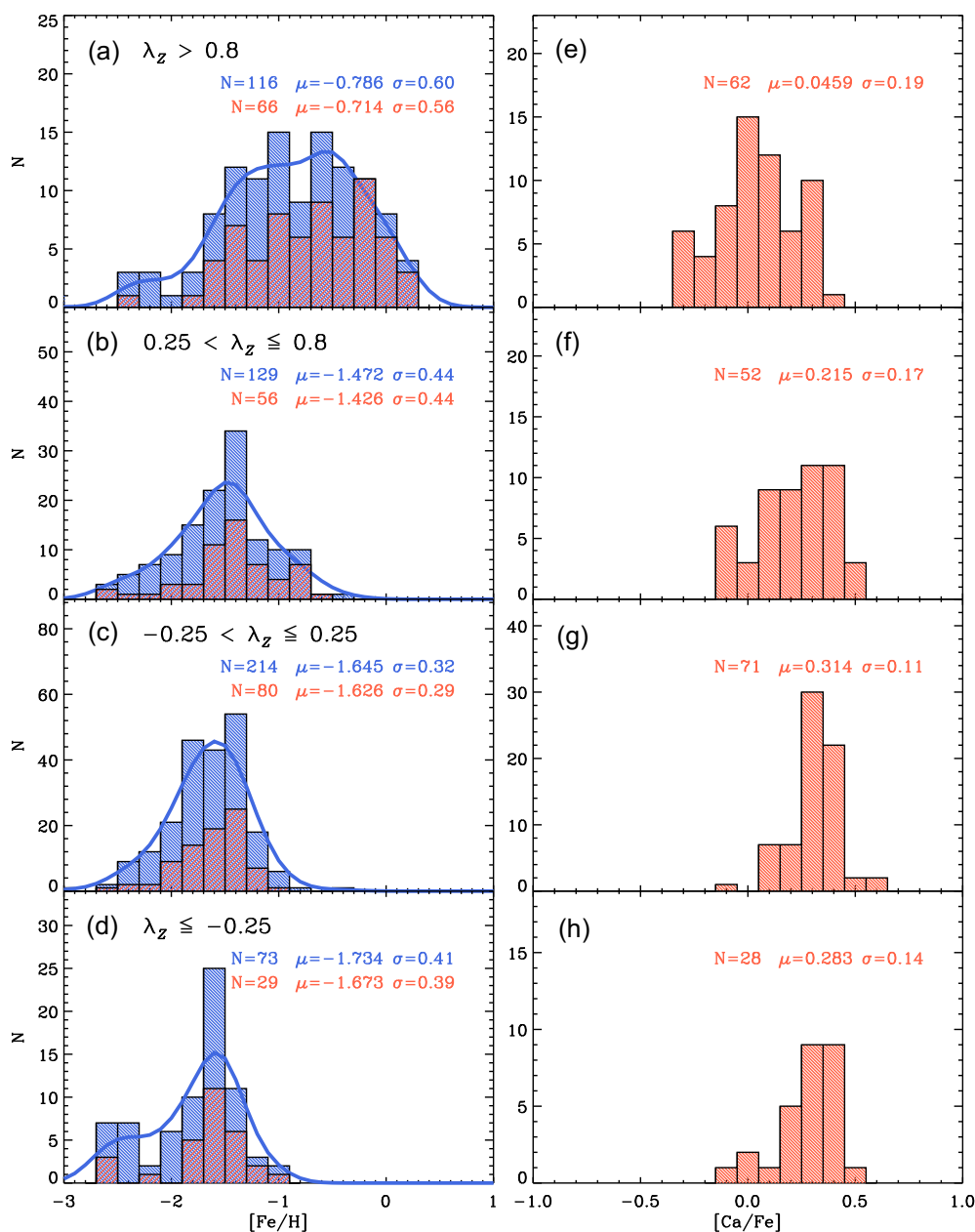


Figure 16. Left – From top to bottom iron distribution function of the entire RRL sample adopted in Fig. 14 for the four kinematic bins defined in Section 5. The red hatched area shows RRLs with iron abundances based on HR spectra, while the blue hatched area the cumulative iron distribution function (HR + LR). The solid blue line displays the running average over the entire sample. The latter was smoothed using a Gaussian kernel with unitary weight and σ equal to the error of the individual estimates. Right – Same as the left, but for the $[Ca/Fe]$ distribution function.

shows an almost flat iron distribution function while the others display an extended metal-poor tail and a sharp decrease in the metal-rich tail as already found by Fabrizio et al. (2021). Note that, this spread in iron abundance is severely underestimated. Preliminary evidence based on HR optical spectra indicates that the RRL with disc kinematics recently discovered by Matsunaga et al. (2023) is more metal-poor than $[Fe/H] \approx -3$ (D’Orazi et al., in preparation). The distributions of $[Ca/Fe]$ for the RRL with HR spectra plotted in the right panels of Fig. 16 further strengthen this evidence. The spread in Ca abundance for RRLs with cold orbits is systematically larger when compared with the other kinematic components.

Fig. 17 shows the Toomre diagram for the RRLs in our sample, where the combination of the velocity in the Galactic centre direction (V_x), and the velocity component perpendicular to the disc plane (V_z) is shown as a function of the velocity of the stars in the direction of the Galactic rotation, V_y . In the left-hand panel, points are colour-coded according to the circularity of the corresponding orbit, while in the right-hand panel, the colours indicate iron abundance. Data plotted in this figure soundly support the results based on the circularity of the orbits plotted in Fig. 14. Our sample RRLs shows a clear gradient, becoming progressively more metal-rich and associated with cooler orbits as they transition from the halo through the thick disc to the thin disc regions. For visual clarity in distinguishing the

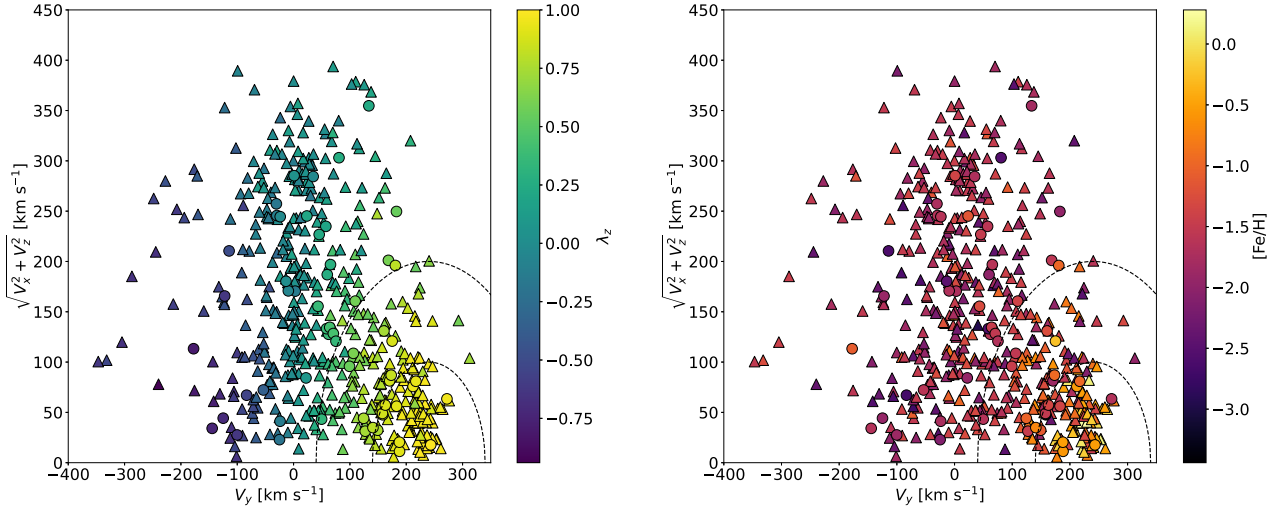


Figure 17. Left – Toomre diagram for the entire RRL sample. The symbols are colour-coded according to the circularity of the orbits (see colour bar on the right). The dashed semi-circles display the regions of the Toomre diagram of thin ($V_y < 50 \text{ km s}^{-1}$) and thick disc ($50 < V_y < 100 \text{ km s}^{-1}$) stars according to the definition by Helmi et al. (2018). Right: Same as the left, but the symbols are colour-coded according to the metallicity $[\text{Fe}/\text{H}]$.

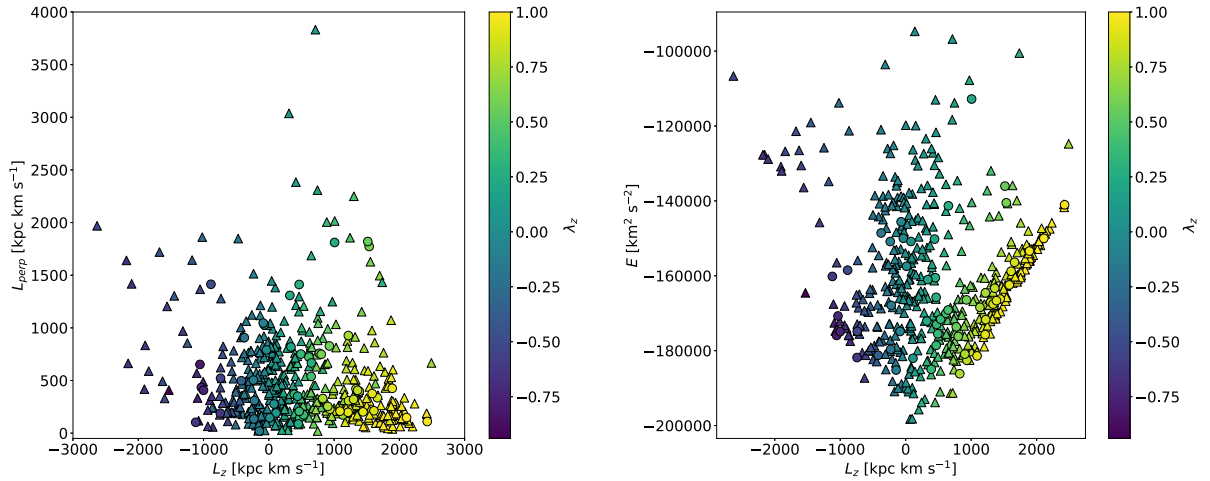


Figure 18. Left – Angular momentum around the z -axis (L_z) versus the angular momentum out of the Galactic plane (L_{\perp}) for the entire RRL sample. The symbols are colour-coded according to the circularity of the orbits. Right: Same as the left, but the angular momentum around the z -axis is plotted versus the total energy.

different sub-samples, Fig. 17 includes semicircles at $V_{\text{LSR}} = 100$ and 200 km s^{-1} . These semicircles, as defined by Helmi et al. (2018), demarcate the boundaries between the thin/thick disc and the halo.

6.1 Kinematic selection of candidate stellar streams

To identify RRLs belonging to possible stellar streams, we adopted two solid diagnostics: the angular momentum and the total energy. There is vast literature concerning the use of these diagnostics to identify stellar streams in the solar vicinity. Dating back to the early identifications of Halo substructures (Helmi et al. 1999) to more recent identifications based on different stellar tracers (Re Fiorentin et al. 2005; Kinman et al. 2007; Koppelman, Helmi & Veljanoski 2018; Zinn et al. 2020; Malhan et al. 2022).

The left panel of Fig. 18 shows the angular momentum around the z -axis (L_z) versus the angular momentum out of the Galactic

plane (L_{\perp}) for the entire RRL sample. The symbols are colour-coded according to the circularity of the orbits (λ_z). As expected, the bulk of the cold, metal-rich RRLs (yellowish symbols) are located at L_z values typical of thin disc stars (see also Fig. 17), while warm/thick disc RRLs (greenish symbols) attain intermediate L_z values and hot/retrograde RRLs (blueish symbols) display a smooth transition toward smaller and negative L_z values. A significant fraction of the RRL sample covers a limited range in L_{\perp} - L_z values. The exceptions are the retrograde RRLs showing two subgroups clustering around $L_z \sim -1500 \text{ kpc km s}^{-1}$ and $L_{\perp} \sim 1500 \text{ kpc km s}^{-1}$, together with a smaller group located at $L_z \sim -2000 \text{ kpc km s}^{-1}$ and $L_{\perp} \sim 500 \text{ kpc km s}^{-1}$. Similar identifications have been provided by Kinman et al. (2007) and Zinn et al. (2020) and more recently by Koppelman et al. (2018) and by Malhan et al. (2022) suggesting the association with the so-called Sequoia stream (Myeong et al. 2019). In the right-hand panel of Fig. 18, we plot the angular momentum around the z -axis (L_z) versus the total energy. As expected, the data

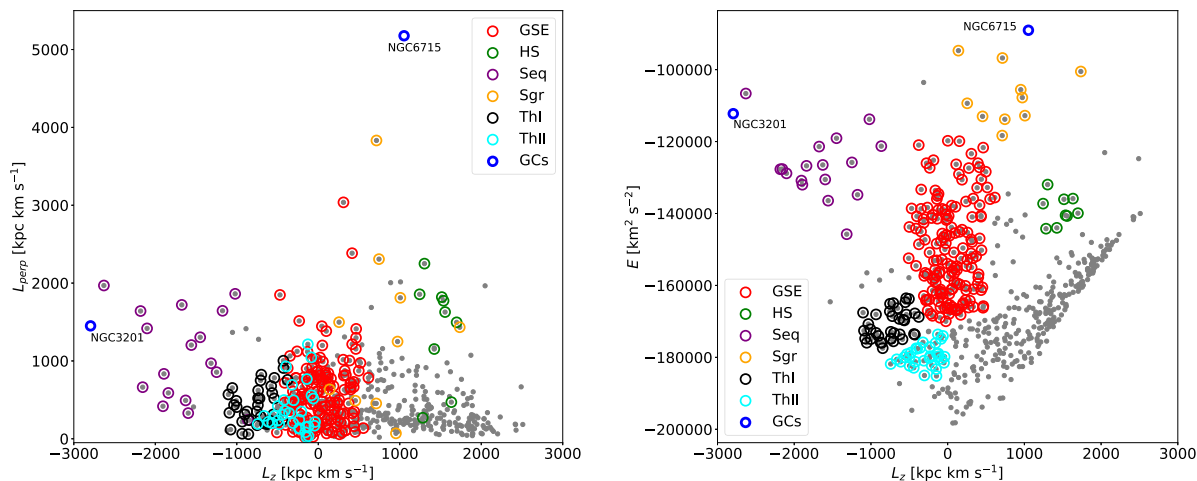


Figure 19. Same as Fig. 18, but with RRLs belonging to the different streams marked with circles of different colours (see labels): Gaia–Sausage–Enceladus (GSE, red), Helmi Stream (HS, green), Sequoia (Seq, brown), Sagittarius (Sgr, purple), Thamnos I (ThI, blue) and Thamnos II (ThII, light blue). The three thick blue circles mark the location of two globular clusters NGC 6715 and NGC 3201. See the text for more details.

display a fan distribution in circularity with a smooth transition when moving from RRLs with cold orbits (yellow) to RRLs with retrograde orbits (dark blue). Furthermore, several overdensities show up across the plane associated with warm, hot, and retrograde orbits.

To properly identify candidate stellar streams, we took advantage of the stream identifications provided by Koppelman et al. (2018), Zinn et al. (2020), and by Malhan et al. (2022). The key idea is to trace back in time their origin using RRLs. Fig. 19 shows the same data as in Fig. 18, but the different streams are marked with different colours. In the following, we discuss in detail the identification of the different streams when moving from RRLs with cold/warm orbits to RRLs with retrograde orbits.

Helmi Stream – Following (Helmi et al. 1999; Zinn et al. 2020) candidate RRLs associated with the HS (green empty circles) plotted in Fig. 19 appear relatively concentrated (candidates are listed in Table A3).

Sagittarius Stream – Following Malhan et al. (2022) candidate RRLs associated with the Sgr stream (purple circles) are located in the top right corner of the L_z – E plane, i.e. at high E values and modest L_z values. The association with the Sgr stream is also supported by the location in the same region of M54 (NGC 6715; Massari, Koppelman & Helmi 2019b). Note that, together with the identifications suggested in the literature, we do have several new candidates, in the high-energy regime, that appear to be associated with the Sgr stream.

Gaia–Sausage–Enceladus Stream – This is the major component of the candidate stellar streams, located in the L_z – E plane at small L_z and energy values. Solid identifications of this stellar stream have been provided by Belokurov et al. (2018) and Helmi et al. (2018), but see also Zinn et al. (2020). Moreover, the current data are indicative of separation from the other candidate stellar streams characterized by lower L_z values (see Thamnos streams).

Sequoia Stream – The candidates to the Seq stream can be easily identified both in the L_z – L_\perp plane and the L_z – E plane, since they are characterized by retrograde orbits (negative L_z values) and small (in absolute sense) energy values (Myeong et al. 2019). The reader interested in a more detailed discussion concerning the occurrence of different sub-groups is referred to Zinn et al. (2020). Ceccarelli et al. (2024) demonstrate that at least two substructures within this area likely originate from the same merger event. It’s important to note

that due to the small sample size of RRL sampling in this region, we refrain from differentiating between the mentioned sub-groups. In passing we note that the current data fully support the association with the globular cluster NGC 3201 (thick blue circle, Massari et al. 2019b), which was also preliminary hinted by Kinman et al. (2012). Moreover, we also identified a new RRL candidate (see data listed in Table A3).

Thamnos Streams – The early identifications of these stellar streams were provided by Koppelman et al. (2019). They are quite prominent in the current L_z – E plane, since they show up as separated local overdensities in the retrograde regime and the lower boundary of the GSE stream. The current data also suggest a few new candidates for the Thamnos II stream (see Table A3). Finally, it is worth mentioning that there is a small (six) RRL group located between the Seq and the Thamnos I stream with retrograde orbits and L_z values similar to the Thamnos streams.

6.2 Characterization of candidate stellar streams

The identification of candidate stellar streams using angular momentum and total energy is robust, but still affected by possible systematics and by the natural uncertainties due, for example, to overlapping structures and complex dynamical processes (see e.g. Belokurov & Kravtsov 2022; Ceccarelli et al. 2024). The identification of local overdensities is subjective and in some cases hampered by limited statistics. The cons of the RRLs as tracers of old stellar populations is that they are roughly two orders of magnitudes less abundant than old main-sequence stars. However, they can be easily recognized and their distances are known with an accuracy better than 3–5 per cent. This means that we can take advantage of this key feature to characterize the preliminary identifications of the stellar streams. The idea is to use Galactocentric distance distributions and elemental abundances to identify the possible presence of a core and to constrain its spatial extent.

Fig. 20 shows the Galactocentric distance distributions for the six candidate stellar streams. Panel (a) shows the distance distribution of RRLs associated with the GSE stream. They are the largest sub-sample (almost one-third) and cover a range in Galactocentric distances similar to the entire RRL sample ($4 < R_G < 11$ kpc) with a modest dispersion (see Table 3). The distribution is skewed toward

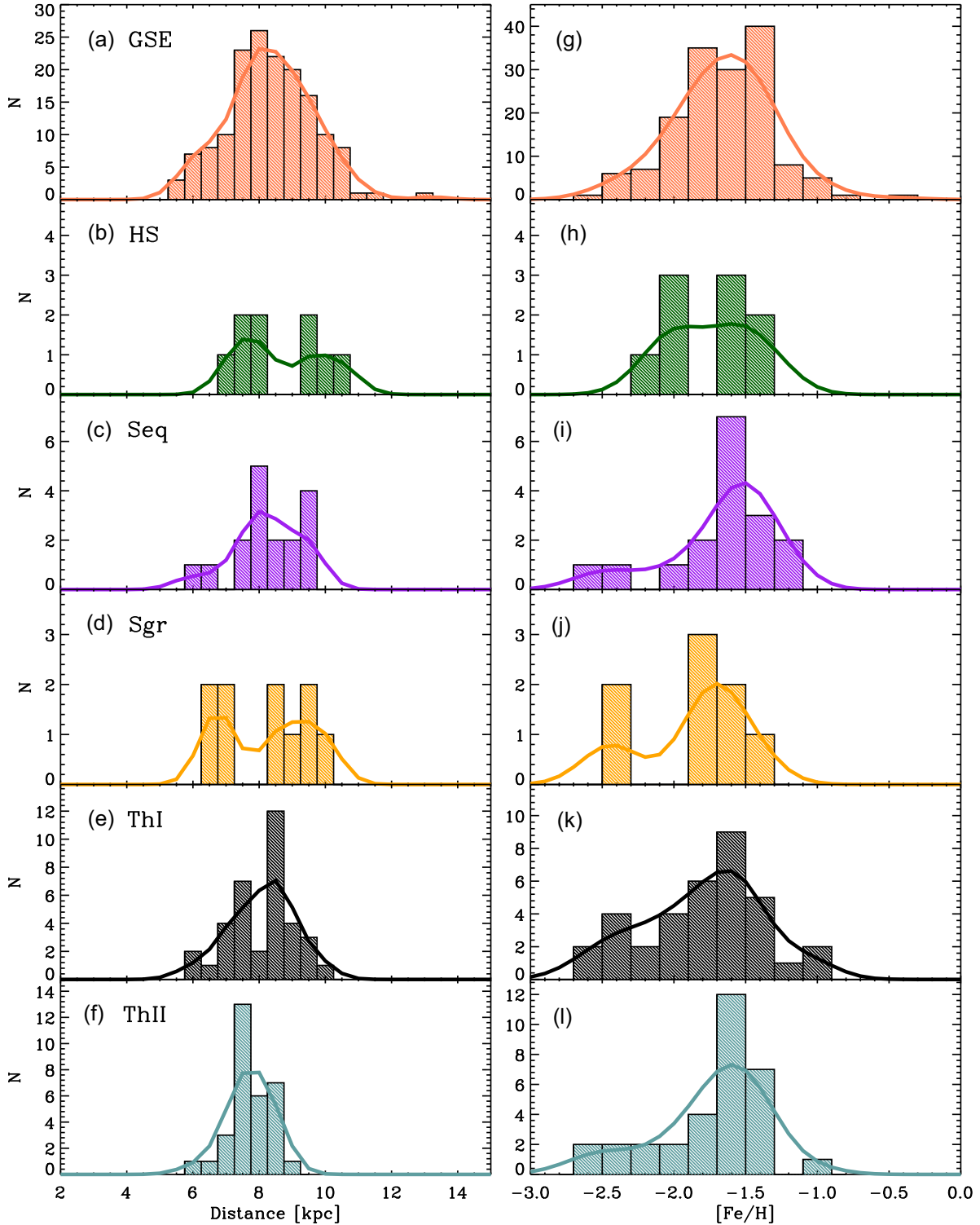


Figure 20. Left: From top to bottom Galactocentric distance distribution of RRLs identified in the different stellar streams. The colour coding is the same as in Fig. 19, and the solid line displays the running average over the entire sample. See text and Table 3 for more details. Right: same as the left, but for the iron distribution function.

larger distances due to an observational bias, field RRLs located either in the bulge or in the inner disc are fainter due to larger reddenings. The core appears to be located across the solar circle ($R_G \sim 8$ kpc). In passing, we also note that the iron distribution (panel g) is quite broad with an extended tail in the metal-poor

regime and a sharp discontinuity in the more metal-rich regime. The weighted mean is $[\text{Fe}/\text{H}] = -1.646 \pm 0.295$, within the uncertainties, similar to the mean abundance of the Halo traced by RRL variables (Fabrizio et al. 2021; Crestani et al. 2021a) and consistent with high-resolution spectroscopic measurement by Ceccarelli et al. (2024).

Table 3. Mean weighted (mean \pm std) Galactocentric distances, iron, calcium and s-process (Y, Ba) abundances for the RRLs associated with the different streams. The number of stars is labelled as n.

Stream	n	distance (kpc)	n	[Fe/H]	n	[Ca/Fe]	n	[Y/Fe]	n	[Ba/Fe]
GSE	156	8.160 \pm 0.856	153	-1.646 \pm 0.295	47	0.314 \pm 0.114	12	-0.069 \pm 0.200	15	-0.110 \pm 0.196
Helmi	9	8.256 \pm 0.537	9	-1.667 \pm 0.293	3	0.252 \pm 0.208	1	0.190 \pm 0.100	2	-0.221 \pm 0.367
Seq	17	8.139 \pm 0.788	17	-1.601 \pm 0.327	5	0.199 \pm 0.126	-	-	2	-0.273 \pm 0.159
Sgr	10	8.271 \pm 0.689	8	-1.867 \pm 0.399	-	-	-	-	-	-
ThI	36	8.275 \pm 0.663	35	-1.761 \pm 0.429	15	0.301 \pm 0.173	4	0.122 \pm 0.368	4	0.078 \pm 0.327
ThII	32	7.948 \pm 0.517	32	-1.735 \pm 0.365	17	0.327 \pm 0.097	2	0.414 \pm 0.313	3	-0.017 \pm 0.398

The weighted mean of the α -element abundance ratio is enhanced ($[\text{Ca}/\text{Fe}] = 0.314 \pm 0.114$), as expected for typical Halo stars. The same outcome applies for s-process elements: within the errors, they display a solar-scaled pattern (see weighted mean abundances in columns 9–11 of Table 3). The current evidence in distance and iron distribution fully supports the findings based on kinematical properties that the GSE stream is associated with a major merging event with a massive dwarf galaxy.

The RRLs in the HS display a dichotomic distribution both in Galactocentric distance (panel b) and in iron abundance (panel h). They are mainly metal-poor, with a moderate enhancement in α -element abundances (see Table 3).

The RRLs in the Sequoia (panel c) stream show trends similar to the GSE stream. Indeed, they are skewed in the same direction and the dispersion in Galactocentric distances are similar. The mean iron abundance (panel i) is also similar and the Ca abundance ratio seems to be slightly less enhanced, but this initial observation is drawn from only five RRLs. Preliminary evidence suggests that RRLs in the Sgr stream have a dichotomic distribution both in Galactocentric distances (panel d) and in iron abundance (panel j). Nevertheless, the limited number of RRLs available prevents definitive conclusions from being drawn at this stage.

The Galactocentric distance distributions of the RRLs associated with Thamnos I (panel e) and Thamnos II (panel f) are also concentrated around the solar circle but show well-defined peaks at ~ 9 and ~ 7 kpc, respectively. This evidence is suggestive of a possible difference in the location of their cores. The iron distribution function of the two streams are quite similar with a main peak located at $[\text{Fe}/\text{H}] \sim -1.7$ and an extended metal-poor tail and sharp decrease in the metal-intermediate-regime ($[\text{Fe}/\text{H}] \sim -1.3$). The $[\text{Ca}/\text{Fe}]$ ratios are enhanced as expected for canonical Halo and thick-disc stars. Abundances of the heavy elements Y and Ba exhibit a large scatter with super solar and solar-scaled patterns.

In closing this section two warnings. (i) – The RRLs are old stellar tracers, their metallicity distributions trace the early chemical enrichment and not the current chemical enrichment. (ii) – The identification of various streams remains an unresolved issue. A recent study by Donlon & Newberg (2023) employed a Bayesian Gaussian regression algorithm and proposed that the GSE stream is composed of four distinct components: Virgo, Cronus, Nereus, and Thamnos. This significant finding prompts the need for new selection criteria that rely on observables not affected by uncertainties in distance and reddening.

7 SUMMARY AND FINAL REMARKS

We performed a detailed abundance analysis of 78 RRLs through high-resolution spectra collected within the DR3 of the GALAH survey. We used a fully consistent NLTE approach to derive spectro-

scopic parameters and abundances for Fe, Ca, Mg, Y, and Ba. The main results of the current investigation are the following:

We find evidence of metal-rich RRLs that have either solar or even sub-solar α -element abundances. This finding fully supports previous measurements based on independent RRL samples provided Sneden et al. (2018) and more recently by Crestani et al. (2021b). However, with respect to previous studies, we provide for the first time heavy-element abundances. The abundance ratios of neutron-capture elements serve as robust diagnostics for determining the origins of metal-rich RRLs. Notably, at a given iron abundance, these elements exhibit underabundance relative to the average stellar populations of the disc (such as those by Bensby et al. 2014). This underabundance suggests that we may be observing an ancient component of the thin disc, in contrast to the comparison stars that cover a broad range in age with typical values of ≈ 7 –8 Gyr (Kilic et al. 2017 and references therein). This discrepancy suggests that the s-process nucleosynthesis did not yet contribute substantially to the chemical evolution at the time the metal-rich RRL stars were formed.

To characterize on a more quantitative basis the nature of metal-rich RRLs, we investigated the kinematical properties of field RRLs. The GALAH sample was complemented with the sample of field RRLs for which our group already performed a detailed chemical abundance using high-resolution spectra (For et al. 2011; Chadid et al. 2017; Sneden et al. 2018; Gilligan et al. 2021; Crestani et al. 2021a, b). Moreover, we took advantage of a large sample of field RRLs for which radial velocities and iron abundance were estimated using low-resolution spectra (Zinn et al. 2020; Fabrizio et al. 2021). To investigate the kinematical properties, we adopted the orbit circularity (λ_z). According to this parameter, stars with $\lambda_z > 0.8$ have cold orbits, while those with $0.25 < \lambda_z \leq 0.8$ have warm orbits, while those with $-0.25 < \lambda_z \leq 0.25$ have hot orbits and those with $\lambda_z \leq -0.25$ are retrograde.

We found that:

(i) – Approximately 10 per cent of the GALAH sample is retrograde. Two of these stars are metal-intermediate ($[\text{Fe}/\text{H}] \sim -1$) and display solar or slightly lower $[\text{Ca}/\text{Fe}]$ abundance ratios. The others are metal-poor and α -enhanced. Two of them appear to be associated with the GSE stream (Belokurov et al. 2018; Helmi et al. 2018).

(ii) – Interestingly, the bulk of the metal-rich RRLs have cold orbits, i.e. a kinematic typical of disc stars. Similar evidence was also suggested based on a smaller RRL sample by Belokurov et al. (2018), Iorio & Belokurov (2021), and by Prudil et al. (2019). Note that, this sub-sample includes almost one-third of the sample and appears to be a relevant component of field RRLs. Moreover, they also have $[\alpha/\text{Fe}]$ abundance ratios either solar or slightly lower. Despite these similarities to the disc stars concerning the iron and the α -element content, the abundances of neutron-capture elements are, at fixed iron abundance, systematically lower than typical disc stars.

(iii) – Metal-intermediate RRLs include roughly one-third of our sample and display a smooth transition from cold to hot orbits. The hot sample is characterized by metal-poor iron abundances similar to the retrograde sub-sample.

These findings based on RRL in the GALAH sample were soundly confirmed by the entire spectroscopic sample we collected. In particular, we found that the distribution of orbit circularity shows two well-defined peaks associated with the metal-rich RRLs with disc kinematics and metal-poor RRLs with halo/bulge kinematics. Moreover, the RRLs with disc kinematics also show a very broad distribution in iron abundance ($-2.5 < [\text{Fe}/\text{H}] < 0$) while the α -element abundances move from solar to α -enhanced. We also investigated the possible impact of the topology of the RRL instability strip on the chemical and kinematic properties of fundamental and first-overtone RRLs but found no clear difference. This finding brings forward three far-reaching consequences.

(i) – The evolutionary channel producing metal-rich RRLs with disc kinematics is canonical. Their number is too large to be the progeny of either binary evolution or stellar collision. This means that they are old low-mass stars in the core-helium burning phase.

(ii) – The chemical composition of metal-rich RRL stars diverges from that of the typical stars in the thin disc, exhibiting deficiencies in both α -elements and neutron-capture elements. Regrettably, the age determinations for thin disc stars, for which uniform measurements of neutron capture elements exist, are exceedingly scarce.

(iii) – The thin disc does not harbour globular clusters, but the current preliminary evidence indicates that it includes an old ($t \geq 10$ Gyr) stellar population. Similar conclusions were reached by Wu et al. (2023, and references therein), who analysed more than 5300 red giant stars by combining *Kepler* and LAMOST data. The authors found that the oldest thin disc stars have an age of $9.5^{(+0.5, +0.5)}_{(-0.4, -0.3)}$ Gyr (the two sources of errors are for random and systematic uncertainties, respectively). Crucially, this result is corroborated by our recent work on a field RRL with thin disc kinematics and iron abundance lower than ≈ -3 (Matsunaga et al. 2023, D’Orazi et al., in preparation). The extended iron distribution function, the range covered in α -element abundances, the neutron capture abundances, the homogeneity in orbit circularity and their distribution in the Toomre diagram point toward an old stellar population with disc kinematics. The current data do not allow us to constrain whether this old stellar component was formed either *in situ* or accreted in the early formation of the Galactic spheroid.

To investigate the kinematical properties of the entire sample, we also performed a selection of candidate stellar streams. This idea was motivated by the fact that we are dealing with an old stellar tracer for which we do have accurate and homogeneous individual distances, radial velocities, and elemental abundances. Following an approach widely adopted in the literature, we took advantage of the total energy (E) of the orbits, the angular momentum along the z -axis (L_z) and of the angular momentum perpendicular (L_\perp). We used the L_z versus L_\perp plane, and in particular, the E versus L_z plane to identify candidate RRLs belonging to six different stellar streams already known in the literature. The key features are the following.

(i) – GSE stream – Firm identifications of this stellar stream were provided by Belokurov et al. (2018) and by Helmi et al. (2018). This is the major component, and indeed, the candidate RRLs are almost one-third of the entire sample and they are located in a well defined region of the E versus L_z plane typical of stars with warm/hot orbits. Moreover and even more importantly, they show a very broad iron distribution function and α -element abundances are enhanced in the metal-poor/metal-intermediate regime and approach solar values or

even lower in the metal-rich regime. The abundances of s -process elements are around solar as expected for typical halo stars. This evidence supports recent findings suggesting that the GSE stream is associated with a major merging event.

(ii) – Helmi stream – The RRLs associated with this stream were recently complemented with new candidates by Zinn et al. (2020). They show up with a well-defined concentration in the E versus L_z plane and they also display a narrow distribution in Galactocentric distance and in iron abundance. More quantitative analyses are hampered by the modest sample size.

(iii) – Seq stream – After the identification of this stream (Myeong et al. 2019), the RRLs associated with this stream have been discussed in detail by Zinn et al. (2020). In particular, they suggested the occurrence of different kinematical sub-groups. The RRLs associated with this stream display an iron distribution function with a main peak similar to RRLs in the GSE and the HS. The same outcome applies to the distribution in Galactocentric distances. Moreover, we support the association with the Galactic globular cluster NGC 3201 (Kinman et al. 2012).

(iv) – Sgr stream – The RRLs associated with this stream display a dichotomic distribution both in Galactocentric distances and in iron abundance. This preliminary evidence should be treated with care since the sample is limited. The current data suggest the association with the Galactic globular M54 (Massari et al. 2019b) considered from the very early identifications of this stream as the core of the Sgr dwarf galaxy (see Ibata et al. 2009 and references therein).

(v) – Thamnos streams – The Galactocentric distance distributions of the RRLs associated to Thamnos I and Thamnos II cluster around the solar circle, but the former one shows a peak at 9 kpc, while the latter one at 7 kpc. This evidence is suggestive of a possible difference in the location of the core of the two streams. The iron distribution functions are similar, moreover, they are α -enhanced and the s -process elements attain solar values. They appear to be typical halo stars, but their orbit circularity and their location in the E versus L_z plane suggest that they are retrograde objects (see however, Giribaldi & Smiljanic 2023, where, based on stellar ages, it is proposed that Thamnos II could be part of an ancient null net rotation structure formed in the Milky Way).

The results of this investigation appear very promising, not only for future spectroscopic developments. The ongoing and near future high-resolution spectroscopic surveys (e.g. WEAVE; Jin et al. 2023; 4MOST; de Jong 2019) will allow us to increase the number of field RRLs with accurate elemental abundances by order(s) of magnitude. Moreover, ongoing (OGLE; Udalski et al. 2004; ZTF; Bellm 2014) and upcoming long-term variability surveys (e.g. Vera Rubin Observatory, Di Criscienzo et al. 2023) will provide firm identifications of RRLs across a significant portion of the Galactic thin disc and the Galactic centre. The kinematics, the pulsation properties and the chemical abundances of these objects will play a key role in assessing on a quantitative basis the early formation of the thin disc and the connection with the different components of the Galactic spheroid.

ACKNOWLEDGEMENTS

This work made extensive use of the SIMBAD, VizieR, and NASA ADS data bases. We are grateful to the reviewer for their careful review and constructive feedback, which have substantially improved the quality of our paper

Parts of this research were supported by the Australian Research Council Centre of Excellence for All Sky Astrophysics in 3 Dimensions (ASTRO 3D), through project number CE170100013. MM

acknowledges financial support from the Spanish Ministry of Science and Innovation (MICINN) through the Spanish State Research Agency, under Severo Ochoa Programme 2020–2023. This research has been supported by the Spanish Ministry of Economy and Competitiveness (MINECO) under the grant AYA2020-118778GB-I00. SWC acknowledges funding from the Australian Research Council through Discovery Projects DP190102431 and DP210101299. This research was supported by use of the Nectar Research Cloud, a collaborative Australian research platform supported by the National Collaborative Research Infrastructure Strategy (NCRIS). MT acknowledges support from the Agencia Estatal de Investigación del Ministerio de Ciencia e Innovación (AEI-MCINN) under grant ‘At the forefront of Galactic Archaeology: evolution of the luminous and dark matter components of the Milky Way and Local Group dwarf galaxies in the Gaia era’ with reference PID2020-118778GB-I00/10.13039/501100011033. VD acknowledges the financial contribution from PRIN MUR 2022 (code 2022YP5ACE) funded by the European Union – NextGenerationEU. Several of us thank the support from Project PRIN MUR 2022 (code 2022ARWP9C) ‘Early Formation and Evolution of Bulge and HalO (EFEBHO)’ (PI: M. Marconi), funded by the European Union – Next Generation EU and by the Large grant INAF 2022 MOVIE (PI: M. Marconi). ML acknowledges the support by the Lendület Program LP2023-10 of the Hungarian Academy of Sciences and the NKFIH excellence grant TKP2021-NKTA-64. TZ acknowledges financial support from the Slovenian Research Agency (research core funding no. P1-0188) and the European Space Agency (Prodex Experiment Arrangement No. 4000142234).

DATA AVAILABILITY

This article’s data are available in the DataCentral at <https://cloud.datacentral.org.au/teamdata/GALAH/public/GALAHDR3/>. The code `TSFitPy` can be downloaded at <https://github.com/TSFitPy-developers/TSFitPy>.

REFERENCES

- Abdurro’uf et al., 2022, *ApJS*, 259, 35
- Ablimit I., Zhao G., Teklimakan U., Shi J.-R., Abdusalam K., 2022, *ApJS*, 258, 20
- Adamow M. M., 2017, in American Astronomical Society Meeting Abstracts #230. p. 216.07
- Baade W., 1958, *Ric. Astron.*, 5, 3
- Beaton R. L. et al., 2018, *Space Sci. Rev.*, 214, 113
- Bellm E., 2014, in Wozniak P. R., Graham M. J., Mahabal A. A., Seaman R., eds, *The Third Hot-wiring the Transient Universe Workshop*. p. 27, available at: <http://www.slac.stanford.edu/econf/C131113.1/proceedings.html>
- Belokurov V., Kravtsov A., 2022, *MNRAS*, 514, 689
- Belokurov V., Deason A. J., Koposov S. E., Catelan M., Erkal D., Drake A. J., Evans N. W., 2018, *MNRAS*, 477, 1472
- Bennett M., Bovy J., 2019, *MNRAS*, 482, 1417
- Bensby T., Feltzing S., Oey M. S., 2014, *A&A*, 562, A71
- Beraldo e Silva L., Debattista V. P., Nidever D., Amarante J. A. S., Garver B., 2021, *MNRAS*, 502, 260
- Bergemann M., Kudritzki R.-P., Würl M., Plez B., Davies B., Gazak Z., 2013, *ApJ*, 764, 115
- Bergemann M., Collet R., Amarsi A. M., Kovalev M., Ruchti G., Magic Z., 2017, *ApJ*, 847, 15
- Bhardwaj A., 2024, *IAU Symp.*, 376, 250
- Blanco-Cuaresma S., 2019, *MNRAS*, 486, 2075
- Bono G., Caputo F., Cassisi S., Icerpi R., Marconi M., 1997, *ApJ*, 483, 811
- Bono G., Dall’Ora M., Caputo F., Coppola G., Genovali K., Marconi M., Piersimoni A. M., Stellingwerf R. F., 2011, in McWilliam A. ed., *Carnegie Observatories Astrophysics Series Vol. 5, RR Lyrae Stars, Metal-Poor Stars, and the Galaxy*. Pasadena, CA, p. 1
- Braga V. F. et al., 2021, *ApJ*, 919, 85
- Buder S. et al., 2021, *MNRAS*, 506, 150
- Busso M., Vescovi D., Palmerini S., Cristallo S., Antonuccio-Delogo V., 2021, *ApJ*, 908, 55
- Cardelli J. A., Clayton G. C., Mathis J. S., 1989, *ApJ*, 345, 245
- Catelan M., 2007, in Roig F., Lopes D., eds, *AIP Conf. Proc. Vol. 930, Graduate School in Astronomy: XI Special Courses at the National Observatory of Rio de Janeiro (XI CCE)*. Am. Inst. Phys., New York, p. 39
- Ceccarelli E. et al., 2024, *A&A*, 684, 21
- Chadid M., Sneden C., Preston G. W., 2017, *ApJ*, 835, 187
- Chen M.-H., Li L.-X., Chen Q.-H., Hu R.-C., Liang E.-W., 2024, *MNRAS*, 529, 1154
- Chopin A., Hirschi R., Meynet G., Ekström S., Chiappini C., Laird A., 2018, *A&A*, 618, A133
- Clementini G., 2024, *IAU Symp.*, 376, 115
- Clementini G. et al., 2019, *A&A*, 622, A60
- Clementini G. et al., 2023, *A&A*, 674, A18
- Cowan J. J., Sneden C., Lawler J. E., Aprahamian A., Wiescher M., Langanke K., Martínez-Pinedo G., Thielemann F.-K., 2021, *Rev. Mod. Phys.*, 93, 015002
- Crestani J. et al., 2021a, *ApJ*, 908, 20
- Crestani J. et al., 2021b, *ApJ*, 914, 10
- de Jong R. S., 2019, *Nat. Astron.*, 3, 574
- De Silva G. M. et al., 2015, *MNRAS*, 449, 2604
- Dékány I., Minniti D., Catelan M., Zoccali M., Saito R. K., Hempel M., Gonzalez O. A., 2013, *ApJ*, 776, L19
- Di Criscienzo M. et al., 2023, *ApJS*, 265, 41
- Donlon T., Newberg H. J., 2023, *ApJ*, 944, 169
- Drake A. J. et al., 2009, *ApJ*, 696, 870
- Drake A. J. et al., 2017, *MNRAS*, 469, 3688
- Drimmel R., Poggio E., 2018, *Res. Notes Am. Astron. Soc.*, 2, 210
- Fabrizio M. et al., 2019, *ApJ*, 882, 169
- Fabrizio M. et al., 2021, *ApJ*, 919, 118
- Feuillet D. K., Feltzing S., Sahlholdt C., Bensby T., 2022, *ApJ*, 934, 21
- Fiorentino G. et al., 2015, *ApJ*, 798, L12
- For B.-Q., Sneden C., Preston G. W., 2011, *ApJS*, 197, 29
- GRAVITY Collaboration, 2023, *A&A*, 615, L15
- Gaia Collaboration, 2023, *A&A*, 674, A1
- Gallagher A. J., Bergemann M., Collet R., Plez B., Leenaerts J., Carlsson M., Yakovleva S. A., Belyaev A. K., 2020, *A&A*, 634, A55
- Gerber J. M., Magg E., Plez B., Bergemann M., Heiter U., Olander T., Hoppe R., 2023, *A&A*, 669, A43
- Gilligan C. K. et al., 2021, *MNRAS*, 503, 4719
- Giribaldi R. E., Smiljanic R., 2023, *A&A*, 673, A18
- Gozha M. L., Marsakov V. A., Koval V. V., 2021, *Astron. Astrophys. Trans.*, 32, 147
- Gustafsson B., Edvardsson B., Eriksson K., Jørgensen U. G., Nordlund Å., Plez B., 2008, *A&A*, 486, 951
- Hansen C. J., Rich R. M., Koch A., Xu S., Kunder A., Ludwig H. G., 2016, *A&A*, 590, A39
- Heiter U. et al., 2021, *A&A*, 645, A106
- Helmi A., White S. D. M., de Zeeuw P. T., Zhao H., 1999, *Nature*, 402, 53
- Helmi A., Babusiaux C., Koppelman H. H., Massari D., Veljanoski J., Brown A. G. A., 2018, *Nature*, 563, 85
- Ibata R. et al., 2009, *ApJ*, 699, L169
- Iorio G., Belokurov V., 2021, *MNRAS*, 502, 5686
- Jayasinghe T. et al., 2019, *MNRAS*, 485, 961
- Jin S. et al., 2024, *MNRAS*, 530, 2688
- Karakas A. I., Lattanzio J. C., 2014, *PASA*, 31, e030
- Kilic M., Munn J. A., Harris H. C., von Hippel T., Liebert J. W., Williams K. A., Jeffery E., DeGennaro S., 2017, *ApJ*, 837, 162
- Kinman T. D., Cacciari C., Bragaglia A., Buzzoni A., Spagna A., 2007, *MNRAS*, 375, 1381
- Kinman T. D., Cacciari C., Bragaglia A., Smart R., Spagna A., 2012, *MNRAS*, 422, 2116

- Koppelman H., Helmi A., Veljanoski J., 2018, *ApJ*, 860, L11
- Koppelman H. H., Helmi A., Massari D., Price-Whelan A. M., Starkenburg T. K., 2019, *A&A*, 631, L9
- Kos J. et al., 2017, *MNRAS*, 464, 1259
- Latham C., Kamenetzky J., Fitzgerald M. T., 2023, *Res. Notes Am. Astron. Soc.*, 7, 68
- Lee D. D., Seung H. S., 1999, *Nature*, 401, 788
- Li C., Binney J., 2022, *MNRAS*, 510, 4706
- Limongi M., Chieffi A., 2018, *ApJS*, 237, 13
- Liu S., Zhao G., Chen Y.-Q., Takeda Y., Honda S., 2013, *Res. Astron. Astrophys.*, 13, 1307
- Longmore A. J., Dixon R., Skillen I., Jameson R. F., Fernley J. A., 1989, in Schmidt E. G., ed., Proc. IAU Colloq. 111: The Use of Pulsating Stars in Fundamental Problems of Astronomy. Lincoln, NE, p. 273
- Lugaro M., Pignatari M., Reifarh R., Wiescher M., 2023, *Ann. Rev. Nucl. Part. Sci.*, 73, 315
- Magg E. et al., 2022, *A&A*, 661, A140
- Magurno D. et al., 2018, *ApJ*, 864, 57
- Magurno D. et al., 2019, *ApJ*, 881, 104
- Malhan K. et al., 2022, *ApJ*, 926, 107
- Marconi M., 2012, Mem. Soc. Astron. Ital. Suppl., 19, 138
- Marconi M. et al., 2015, *ApJ*, 808, 50
- Marconi M., Bono G., Pietrinferni A., Braga V. F., Castellani M., Stellingwerf R. F., 2018, *ApJ*, 864, L13
- Marsakov V. A., Gozha M. L., Koval V. V., 2018, *Astron. Rep.*, 62, 50
- Marsakov V. A., Gozha M. L., Koval’ V. V., 2019, *Astron. Rep.*, 63, 203
- Mashonkina L. et al., 2008, *A&A*, 478, 529
- Mashonkina L. L., Neretina M. D., Sitnova T. M., Pakhomov Y. V., 2019, *Astron. Rep.*, 63, 726
- Massari D., Koppelman H. H., Helmi A., 2019a, *A&A*, 630, L4
- Massari D., Koppelman H. H., Helmi A., 2019b, *A&A*, 630, L4
- Matsunaga N. et al., 2023, *ApJ*, 954, 198
- McMillan P. J., 2017, *MNRAS*, 465, 76
- Minelli A., Mucciarelli A., Romano D., Bellazzini M., Origlia L., Ferraro F. R., 2021, *ApJ*, 910, 114
- Monachesi A. et al., 2019, *MNRAS*, 485, 2589
- Mucciarelli A., Minelli A., Bellazzini M., Lardo C., Romano D., Origlia L., Ferraro F. R., 2023a, *A&A*, 671, A124
- Mucciarelli A., Minelli A., Lardo C., Massari D., Bellazzini M., Romano D., Origlia L., Ferraro F. R., 2023b, *A&A*, 677, A61
- Mullen J. P. et al., 2021, *ApJ*, 912, 144
- Mullen J. P. et al., 2022, *ApJ*, 931, 131
- Myeong G. C., Vasiliev E., Iorio G., Evans N. W., Belokurov V., 2019, *MNRAS*, 488, 1235
- Neeley J. R. et al., 2017, *ApJ*, 841, 84
- Neeley J. R. et al., 2019, *MNRAS*, 490, 4254
- Pietrukowicz P. et al., 2020, *AcA*, 70, 121
- Pignatari M., Gallino R., Heil M., Wiescher M., Käppeler F., Herwig F., Bisterzo S., 2010, *ApJ*, 710, 1557
- Plez B., 2012, Astrophysics Source Code Library, record ascl:1205.004
- Pojmanski G., 1997, *AcA*, 47, 467
- Preston G. W., 1959, *ApJ*, 130, 507
- Preston G. W., 1964, *ARA&A*, 2, 23
- Preston G. W., Sneden C., Chadid M., Thompson I. B., Shectman S. A., 2019, *AJ*, 157, 153
- Prudil Z., Dékány I., Catelan M., Smolec R., Grebel E. K., Skarka M., 2019, *MNRAS*, 484, 4833
- Prudil Z., Dékány I., Grebel E. K., Kunder A., 2020, *MNRAS*, 492, 3408
- Randich S. et al., 2022, *A&A*, 666, A121
- Re Fiorentin P., Helmi A., Lattanzi M. G., Spagna A., 2005, *A&A*, 439, 551
- Reichert M., Hansen C. J., Hanke M., Skúladóttir Á., Arcones A., Grebel E. K., 2020, *A&A*, 641, A127
- Reid M. J., Brunthaler A., 2004, *ApJ*, 616, 872
- Ruchtig G. R., Bergemann M., Serenelli A., Casagrande L., Lind K., 2013, *MNRAS*, 429, 126
- Sandage A., 1962, in McVittie G. C., ed., Proc. IAU Symp. 15, Problems of Extra-Galactic Research. New York, p. 359
- Santucci G. et al., 2023, *MNRAS*, 521, 2671
- Schlafly E. F., Finkbeiner D. P., 2011, *ApJ*, 737, 103
- Schönrich R., Binney J., Dehnen W., 2010, *MNRAS*, 403, 1829
- Semenova E. et al., 2020, *A&A*, 643, A164
- Sheinis A. et al., 2015, *J. Astron. Telesc. Instrum. Syst.*, 1, 035002
- Shi J. R., Gehren T., Mashonkina L., Zhao G., 2009, *A&A*, 503, 533
- Snaith O. N., Bailin J., Gibson B. K., Bell E. F., Stinson G., Valluri M., Wadsley J., Couchman H., 2016, *MNRAS*, 456, 3119
- Sneden C. A., 1973, PhD thesis, University of Texas, Austin
- Sneden C. et al., 2018, *AJ*, 155, 45
- Soszyński I. et al., 2011, *AcA*, 61, 1
- Storm N., Bergemann M., 2023, *MNRAS*, 525, 3718
- Tolstoy E., Battaglia G., Cole A., 2008, in Hunt L. K., Madden S. C., Schneider R., eds, Proc. IAU Symp. 255, Low-Metallicity Star Formation: From the First Stars to Dwarf Galaxies. New York, p. 310
- Udalski A., Szymanski M. K., Kubiak M., Pietrzynski G., Soszynski I., Zebrun K., Szewczyk O., Wyrzykowski L., 2004, *AcA*, 54, 313
- Vasiliev E., 2019, *MNRAS*, 482, 1525
- Walker A. R., Terndrup D. M., 1991, *ApJ*, 378, 119
- Wheeler A. J., Abruzzo M. W., Casey A. R., Ness M. K., 2023, *AJ*, 165, 68
- Wright E. L. et al., 2010, *AJ*, 140, 1868
- Wheeler A. J., Casey A. R., Abruzzo M. W., 2024, *AJ*, 167, 12
- Wu Y., Xiang M., Zhao G., Chen Y., Bi S., Li Y., 2023, *MNRAS*, 520, 1913
- Zhu L. et al., 2018, *MNRAS*, 473, 3000
- Zinn R., Chen X., Layden A. C., Casetti-Dinescu D. I., 2020, *MNRAS*, 492, 2161

APPENDIX A: RR LYRAE SAMPLE AND PROPERTIES

Table A1. Information on our sample RR Lyrae stars, including GALAH DR3 and Gaia DR3 identifiers, pulsation modes, periods, mean magnitudes, amplitudes and reference epochs. The Source column indicates whether the lightcurve, mean magnitude and amplitude come from ASASSN-V (0), Gaia DR3 (1) or Catalina (2). For 0 and 2, these are provided in the V band, for 1, in the G band.

Gaia DR3 ID	GALAH ID	myRRLyrSourceId	Type	P d	<mag> mag	Ampl mag	Source	T_{max}	T_{ris}
144809087288307584	181225002601109	CSS_J043442.9+214621	RRab	0.390592	12.799	1.21	0	2456596.3187	2456595.8920
666167814367063296	170122003601291	CSS_J084038.7+231550	RRe	0.295777	11.653	0.50	0	2456598.0724	2456598.0300
2621577222057910528	140707003101048	CSS_J223052.5-074240	RRab	0.525980	13.398	1.07	0	2456629.9475	2456629.8984
2622375506154471680	140707003101129	BN Aqr	RRab	0.469677	12.538	1.26	0	2456629.8657	2456629.8233
2683960526815908224	170907003601069	CSS_J220237.0+034216	RRab	0.549587	13.055	0.93	0	2456231.9541	2456231.9022
269754253435739776	171101001201268	ASAS J215635+0621.3	RRe	0.338949	12.065	0.39	0	2456597.8348	2456597.7711
271014512135598464	160815004301176	CSS_J222314.6+064802	RRab	0.542516	13.986	0.87	0	2456593.9129	2456593.8602
3201175430791113600	181222001801012	CSS_J044752.9-112047	RRab	0.640042	12.975	0.40	0	2456631.3672	2456631.2903
3230309671428428928	171003005101270	CSS_J043640.7-044014	RRab	0.630553	12.696	0.29	0	2456594.4686	2456593.7368
3323274788307690112	151219003101110	CSS_J043354.9-002532	RRab	0.487685	12.692	1.01	0	2456626.0455	2456625.9987
3406613410300235904	140118002001313	ASAS J060355+0814.5	RRab	0.655919	12.732	1.00	0	2457008.3687	2457008.3043
3471095334863875456	170216003301235	ASAS J045648+1818.3	RRe	0.236864	11.678	0.31	0	2456001.0366	2456000.7479
3479598373678136832	160415003101009	SSS_J123842.8-291327	RRab	0.778209	13.450	0.69	0	2456793.0069	2456792.9248
3892831505236595456	150490002101115	DT Hya	RRab	0.567980	13.015	0.98	0	2456785.1237	2456784.5018
4118543955178309376	170507010601283	CSS_J115945.2+025147	RRab	0.767693	12.068	0.43	1	2456876.4348	2456875.5660
4179431168210587648	151009001601156	ASASSN-V J174848.92-215251.6	RRab	0.523978	11.873	0.92	0	2457017.3439	2457017.2792
4356714327124981632	160514003801381	NSVS 16880684	RRab	0.356331	12.658	0.33	1	2456917.3439	2456917.2792
4377598863300947584	170711003001180	PSI 106611	RRab	0.571050	13.304	0.66	0	2456677.3137	2456677.2524
4387211137548084352	160421005101223	CSS_J165135.0-040010	RRab	0.445715	14.396	1.09	0	2456675.4004	2456674.9123
4476491413005810176	160817002101389	NSVS 13688631	RRab	0.737684	12.247	0.42	0	2456445.6577	2456444.8098
4649015060967755520	150208002701190	PSI 137119	RRab	0.665744	13.869	0.28	0	2456676.6715	2456675.8995
4705269305654137728	170905003501244	ASAS J051623-7527.4	RRab	0.602574	12.761	1.00	1	2456899.7921	2456894.8088
4717044869029445632	171001002901257	AG Tuc	RRab	0.537899	13.012	1.01	0	2456809.9257	2456809.8759
473795661811744832	161117003501393	ASAS J013055-5935.2	RRab	0.572881	12.049	0.72	1	2456869.0362	2456868.4045
4894040677457410944	150902003701106	SSS_J023019.4-590805	RRab	0.505065	13.613	1.09	0	2456848.9581	2456848.9108
5377248172118234624	160525002701364	SSS_J044525.5-245536	RRab	0.557873	13.290	0.90	0	2456784.8975	2456784.8417
5378134722086771840	170603002101348	SSS_J111536.5-423619	RRab	0.592547	13.728	0.63	0	2456793.0803	2456792.4260
5380885768898706688	170511001101394	SSS_J115007.0-443135	RRab	0.397422	13.119	0.99	0	2456792.5790	2456792.5790
5420008488562024064	190211002801043	KS Cen	RRab	0.535917	12.455	1.21	0	2456784.7542	2456784.7023
5420283950583950464	140414002601184	SSS_J095706.0-391727	RRe	0.356108	13.004	0.07	3	2458165.8780	2458165.7950
5469689165544998400	160129005201291	ASASSN-V J101104.07-400651.4	RRab	0.467723	13.595	1.27	0	2456792.3786	2456792.3786
5500275203911641344	171206005101348	SSS_J104201.2-262653	RRe	0.220926	12.139	0.34	0	2456785.5643	2456785.5151
5583138458927986816	161117005201008	ASAS J061233-5402.6	RRab	0.586934	13.475	0.62	0	2456785.8740	2456785.8110
5721724473609473024	150210003201109	SSS_J064733.9-324722	RRab	0.587727	13.629	0.60	2	2453587.3276	2453587.3276
579086204394382784	170511001601385	ASAS J081624-1513.4	RRab	0.622437	13.072	0.52	0	2457455.9435	2457455.8820
5811341925478455680	160813002101375	ASASSN-V J131525.38-752744.2	RRab	0.544882	14.061	0.49	1	2456902.4482	2456902.4482
5820212372985755648	140312004501064	SSS_J173422.2-690828	RRab	0.588727	13.629	0.60	2	2453587.3276	2453587.3276
5821920567383108224	160327006101183	ASAS J153830-6906.4	RRab	0.622437	13.072	0.52	0	2457455.9435	2457455.8820
6029536215017666560	160326001601102	UCAC4 121-145252	RRab	0.405418	13.663	0.84	1	2456902.4877	2456902.4482
6095101210837181056	170516003101297	SSS_J154651.6-380040	RRab	0.576051	12.958	1.01	0	2457456.8897	2457456.8340
6081475783346889600	170508003301387	ASASSN-V J162036.29-322435.7	RRab	0.502336	14.254	1.13	0	2457457.3335	2457456.7838
6096455220523450112	190206007201270	ASASSN-V J130646.56-501617.8	RRab	0.508149	13.795	0.75	0	2457423.1197	2457422.5578
6104846246589810304	160418004101394	SSS_J142022.9-443200	RRab	0.607117	11.948	0.57	0	2457458.0988	2457458.0274
6109120799902812928	170413004101159	ASAS J143814-4025.6	RRe	0.374718	13.262	0.45	0	2457457.9696	2457457.8959
6120342346853804160	160328004201274	ASASSN-V J135041.67-421434.7	RRab	0.332638	12.776	0.77	1	2456899.2747	2456899.2287
		SSS_J142437.2-332942	RRe	0.184775	12.578	0.49	0	2456790.7022	2456790.4943

Table A1 – *continued*

Gaia DR3 ID	GALAH ID	myRRLyrSourceId	Type	P d	<mag> mag	Ampl mag	Source	T_{max}	T_{ris}
612158895681859760	160424004201158	SSS_J135658.5-364111	RRab	0.703782	13.187	0.70	0	2456794.0784	2456793.3001
6137933300244848384	160519003601266	SSS_J131629.2-410407	RRab	0.836563	13.194	0.24	1	2456897.6068	2456897.4721
6162709690968204288	150607002601302	SSS_J132745.4-374659	RRab	0.548049	13.008	0.90	0	2456793.8831	2456793.8289
6180274359158473728	160415003601070	ASASSN-V J130615.31-323202.9	RRc	0.330064	13.502	0.06	3	2457457.9144	2457458.1721
6182771968540082176	170515003101037	SSS_J131301.2-292531	RRab	0.700974	13.040	0.53	1	2456897.6910	2456896.9053
622538099055363456	170531003301371	SSS_J145702.0-264238	RRab	0.586276	13.380	0.49	1	2456904.0275	2456903.9300
626585956422527216	160513002601168	XX Lib	RRab	0.698501	12.375	0.75	1	2456904.8504	2456904.0831
6242022966539339136	140414004601373	SSS_J160733.6-240311	RRab	0.576510	12.840	0.62	1	2456908.1175	2456907.4852
6273401001165886336	170415004101377	SSS_J142624.1-225311	RRab	0.600104	13.645	0.39	2	2453478.8643	2453478.7865
6367478755094103808	170905002101379	ASAS J192639-7438.6	RRc	0.316734	12.432	0.39	0	2456794.9731	2456794.5781
6378877082899249664	150830004601021	AR Oct	RRab	0.394029	12.769	1.23	0	2456792.0435	2456792.0064
6409071321466282752	161008003001285	SSS_J215601.0-612912	RRab	0.616088	12.752	1.10	0	2456790.0647	2456790.0068
6409095201484462208	150828003701073	ASAS J215855-6109.1	RRab	0.802121	12.665	0.16	0	2456790.1041	2456789.9391
6434640155133754368	170516004101029	ASASSN-V J185553.56-664412.0	RRab	0.719612	13.363	0.94	0	2456793.3233	2456792.5323
6454841894587413376	160816003201145	SSS_J203305.8-611320	RRab	0.577596	13.945	0.80	0	2456791.1779	2456791.1070
6463159287733222016	150603004301337	SSS_J211324.5-552407	RRab	0.646437	13.784	0.31	0	2456793.2197	2456792.4753
6473684637667905280	170614004101002	SSS_J201425.0-525542	RRab	0.575418	13.237	0.41	0	2456790.1162	2456790.0458
6562247309988278144	140808003201227	SSS_J213829.6-490054	RRab	0.477468	13.686	0.91	0	2456793.0378	2456792.5084
6564092943335079808	140811004501392	SSS_J214753.4-471332	RRab	0.632508	13.799	0.77	0	2456790.2502	2456790.1856
6637089279786058880	140611004001172	SSS_J190236.4-563640	RRab	0.638228	13.160	0.34	0	2456785.3688	2456785.2804
6638021596927943808	180628003301156	SSS_J190001.9-551546	RRab	0.460542	13.608	0.97	0	2456795.2034	2456794.6989
6640222746188019200	150603003801282	SSS_J192907.7-554517	RRc	0.343012	13.078	0.42	0	2456784.9368	2456784.8515
6650047986394047104	170805003101128	ASAS J184324-5458.9	RRab	0.359691	13.196	1.29	0	2456784.9482	2456784.9147
6664639188589394688	170713004101098	SSS_J191941.6-443402	RRc	0.247099	13.408	0.26	0	2456814.9134	2456814.8569
6665135721170434816	170713004101347	SSS_J192157.1-432821	RRab	0.593109	12.143	0.49	0	2456790.1657	2456789.5019
6674570703462167680	170905002601269	ASAS J203616-4628.1	RRab	0.497461	13.566	0.81	0	2456790.2918	2456789.7442
6679308288613240064	160916001801011	SSS_J202812.2-423609	RRab	0.479459	13.719	1.03	0	2456792.9185	2456792.3870
6681635649786400384	150705005401263	SSS_J203652.4-391206	RRab	0.654473	14.172	0.48	0	2456793.1912	2456793.0987
66819444303315818624	150705005401344	SSS_J204110.0-390818	RRab	0.522306	13.403	1.07	0	2456792.9871	2456792.9386
6694638955332768512	160530005501015	ASAS J202817-3806.6	RRc	0.244849	13.215	0.40	0	2456789.9191	2456789.8588
6698926702788332416	170507011701145	ASAS J195927-3400.1	RRc	0.379658	12.372	0.60	0	2456790.0545	2456789.9786
6730211038418525056	170710002201295	V0413 CrA	RRab	0.589343	10.591	0.60	0	2456797.3124	2456796.6565
6768220266332023040	151008001601166	ASAS J193559-2418.6	RRab	0.628529	13.100	0.35	0	2456790.1843	2456789.4531
6795546531894178816	171003002101302	SSS_J205254.6-285212	RRab	0.632154	13.913	0.66	0	2456788.9960	2456788.9308

Table A2. Kinematics properties of our RRLs.

Gaia DR3 ID	HJD(begin)	HJD(end)	$\langle\phi_{Tris}\rangle$	$\langle\phi_{Trmax}\rangle$	distance pc	RV km/s	v_y km/s
144809087288307584	2458477.9938	2458478.0355	0.6396	0.5470	1579 ± 55	85.14 ± 0.51	70.24 ± 2.45
666167814367063296	2457776.0683	2457776.1100	0.9251	0.7815	1535 ± 24	-117.35 ± 2.71	-124.36 ± 3.01
2621577222057910528	2456846.2095	2456846.2512	0.2930	0.1996	2981 ± 169	-60.68 ± 1.48	-45.37 ± 2.73
2622375506154471680	2456846.2096	2456846.2513	0.7574	0.6672	2334 ± 140	-128.73 ± 1.82	-151.05 ± 3.05
2683960526815908224	2458004.0651	2458004.1068	0.5731	0.4786	3147 ± 49	-212.13 ± 1.97	-221.77 ± 2.93
2697542553435739776	2458058.9482	2458058.9899	0.9682	0.7801	1598 ± 48	-299.83 ± 3.09	-302.98 ± 3.26
271045213353598464	2457616.1448	2457616.1864	0.3766	0.2795	2604 ± 65	-140.15 ± 0.91	-133.49 ± 2.31
3181149548774349824	2458474.9484	2458474.9901	0.5610	0.4407	2390 ± 95	222.88 ± 0.87	215.46 ± 1.90
3201175430791113600	2458030.2157	2458030.2574	0.1586	0.9980	2284 ± 74	-61.70 ± 2.56	-39.93 ± 3.02
3230309671428428928	2457376.0569	2457376.0986	0.0410	0.9451	1852 ± 70	32.21 ± 3.51	61.76 ± 4.16
3323274788307690112	2456676.0137	2456676.0553	0.4287	0.3304	2087 ± 85	28.84 ± 2.13	31.47 ± 3.04
34066134103000235904	2457803.9068	2457803.9485	0.7278	0.5092	811 ± 12	90.75 ± 0.89	84.10 ± 1.23
3471095334863875456	2457801.1824	2457801.2241	0.6400	0.5346	4384 ± 356	214.82 ± 1.22	202.92 ± 1.89
3479598373678136832	2457494.0181	2457494.0597	0.2301	0.1351	3121 ± 50	59.80 ± 1.67	81.86 ± 2.72
4118543955178309376	2457121.9123	2457121.9540	0.9187	0.7870	2146 ± 131	204.26 ± 2.89	180.21 ± 3.16
4179431168210587648	2457304.8828	2457304.9244	0.6847	0.5902	875 ± 14	16.39 ± 1.93	0.60 ± 2.90
4356714327124981632	2457523.0586	2457523.1003	0.8199	0.6383	2239 ± 102	-149.51 ± 0.82	-157.26 ± 1.21
4377598863300947584	2457945.9675	2457946.0092	0.7680	0.6728	2186 ± 89	-7.78 ± 1.86	16.31 ± 2.65
4387211137548084352	2457500.2115	2457500.2532	0.7235	0.5742	3573 ± 296	-57.80 ± 0.85	-79.32 ± 2.46
4476491413005810176	2457617.9238	2457617.9655	0.2101	0.0537	1624 ± 38	-184.85 ± 1.99	-198.11 ± 2.36
4649015060967755520	2457061.9095	2457061.9511	0.3845	0.2663	3417 ± 124	98.50 ± 2.19	105.42 ± 2.56
4705269305654137728	2458002.1540	2458002.1957	0.5479	0.4559	3232 ± 150	187.17 ± 1.57	178.74 ± 2.67
4717044869029445632	2458028.1148	2458028.1565	0.8470	0.7544	3218 ± 51	135.46 ± 0.63	113.08 ± 2.32
473795661817144832	2457710.0254	2457710.0670	0.1392	0.0365	1903 ± 50	92.35 ± 5.42	120.56 ± 5.76
4894040677457410944	2457268.2982	2457268.3399	0.4046	0.3108	4232 ± 63	293.64 ± 1.04	298.16 ± 2.53
5377248172118234624	2457533.8594	2457533.9011	0.6689	0.5688	3344 ± 54	183.06 ± 1.03	166.84 ± 2.32
5378134722086771840	2457907.8635	2457907.9052	0.4818	0.3776	3291 ± 181	189.60 ± 1.36	187.41 ± 2.31
5380885768898706688	2457884.9340	2457884.9756	0.6516	0.5414	2380 ± 76	-19.38 ± 0.45	-33.83 ± 2.27
5420008488562024064	2458526.0867	2458526.1284	0.3908	0.2940	2325 ± 37	257.27 ± 1.81	263.38 ± 3.01
5420283950583950464	2456761.9448	2456761.9865	0.8541	0.6208	1474 ± 31	67.70 ± 1.52	65.52 ± 1.54
5469689165544998400	2457417.1770	2457417.2186	0.8741	0.7815	4063 ± 62	136.58 ± 0.76	111.41 ± 2.57
5500275203911641344	2458094.2102	2458094.2518	0.7845	0.5616	1493 ± 29	101.36 ± 0.46	93.56 ± 1.03
5583138458927986816	2457710.2116	2457710.2533	0.9996	0.8922	3327 ± 127	150.50 ± 1.42	148.58 ± 2.34
5721724473609473024	2457064.0265	2457064.0681	0.6885	0.5921	3139 ± 50	30.85 ± 0.60	13.91 ± 2.37
5790862043943782784	2457884.9844	2457885.0261	0.9180	0.8020	3333 ± 165	17.32 ± 1.18	-2.54 ± 2.16
5811341925478455680	2457613.8864	2457613.9280	0.4636	0.3677	3525 ± 180	140.87 ± 1.10	140.19 ± 2.15
5820212372985755648	2456729.2493	2456729.2909	0.6346	0.5357	2344 ± 83	-17.85 ± 0.82	-30.09 ± 1.96
5821920567383108224	2457475.2462	2457475.2879	0.9093	0.8120	2872 ± 133	-11.50 ± 0.64	-34.15 ± 2.20
6009536215017666560	2457474.2372	2457474.2789	0.2475	0.1508	1938 ± 72	-100.57 ± 1.43	-79.92 ± 2.60
6025101210857181056	2457890.1071	2457890.1487	0.6581	0.5637	2890 ± 181	-22.59 ± 0.74	-38.13 ± 2.45
6081475783346899600	2457882.0293	2457882.0710	0.2477	0.1420	2637 ± 119	92.68 ± 0.90	110.40 ± 2.21
6096455220523450112	2458521.2590	2458521.3007	0.3129	0.1953	1456 ± 35	131.55 ± 1.04	143.65 ± 2.09
6104846246589810304	2457497.1301	2457497.1718	0.7590	0.5623	3485 ± 52	-124.21 ± 0.81	-134.02 ± 1.44
6109120799902812928	2457857.1145	2457857.1562	0.7281	0.5896	2056 ± 83	9.58 ± 0.30	-7.61 ± 2.06
6120342346853804160	2457476.1962	2457476.2378	0.1228	0.9978	2252 ± 85	-3.44 ± 1.67	12.60 ± 2.10

Table A2 – *continued*

Gaia DR3 ID	HJD(begin)	HJD(end)	$\langle \phi_{Tris} \rangle$	$\langle \phi_{Tmax} \rangle$	distance pc	RV km/s	v_y km/s
612158895681859760	2457503.0730	2457503.1147	0.5426	0.4367	3498 ± 63	271.08 ± 2.11	265.14 ± 2.56
6137933300244848384	2457527.9897	2457528.0313	0.7253	0.5643	3460 ± 190	196.12 ± 0.98	183.93 ± 1.53
6162709690968204288	2457180.9302	2457180.9718	0.3641	0.2651	2498 ± 110	179.40 ± 1.93	187.29 ± 2.89
6180274359158473728	2457494.0569	2457494.0986	0.7836	0.5644	1700 ± 55	-22.20 ± 1.28	-24.19 ± 1.30
6182771968540082176	2457888.9837	2457889.0254	0.3157	0.1948	3512 ± 64	11.02 ± 1.18	23.35 ± 1.79
622538099055363456	2457904.9774	2457905.0191	0.5025	0.3363	2839 ± 189	-60.34 ± 1.52	-63.94 ± 2.32
6226585956422527616	2457522.0118	2457522.0535	0.6790	0.5805	2273 ± 80	104.09 ± 4.88	88.35 ± 5.26
6242022966539339136	2456762.1564	2456762.1980	0.9524	0.8556	2277 ± 93	87.10 ± 1.32	65.18 ± 2.28
6273401001165886336	2457859.1199	2457859.1616	0.3313	0.2016	3727 ± 310	-59.76 ± 1.18	-50.02 ± 2.05
6367478755094103808	2458001.9410	2458001.9827	0.9815	0.7346	2217 ± 82	4.38 ± 2.28	2.25 ± 2.51
6378877082899249664	2457265.0970	2457265.1386	0.7024	0.6083	2051 ± 82	-7.48 ± 0.46	-26.24 ± 2.46
6409071321466282752	2457669.9739	2457670.0155	0.3488	0.2548	3071 ± 52	171.30 ± 2.45	182.48 ± 3.32
6409095201484462208	2457263.0445	2457263.0862	0.8439	0.6382	2355 ± 64	64.47 ± 4.16	48.60 ± 4.31
6434640155133754368	2457890.2094	2457890.2510	0.4014	0.3023	4142 ± 78	184.54 ± 1.02	191.17 ± 1.89
6454841894587413376	2457617.0217	2457617.0634	0.9534	0.8305	4528 ± 414	-84.16 ± 0.79	-107.67 ± 2.15
6463159287733222016	2457177.2618	2457177.3034	0.2738	0.1224	3435 ± 176	76.04 ± 1.24	89.55 ± 2.03
6473684637667905280	2457919.1806	2457919.2223	0.3233	0.2010	3103 ± 173	-73.40 ± 0.53	-62.96 ± 1.77
6562247309988278144	2456878.1021	2456878.1437	0.3094	0.2008	3291 ± 160	-1.21 ± 1.22	11.65 ± 2.48
6564092943335079808	2456881.1618	2456881.2034	0.8668	0.7647	3753 ± 227	-78.15 ± 0.58	-98.70 ± 2.06
6637089279786058880	2456820.1916	2456820.2332	0.7328	0.5942	2278 ± 116	340.00 ± 0.90	325.55 ± 1.87
6638021596927943808	2458298.1093	2458298.1510	0.4818	0.3863	3597 ± 55	48.94 ± 0.93	46.20 ± 2.39
6640222746188019200	2457177.2098	2457177.2515	0.9225	0.6737	3316 ± 182	-107.25 ± 1.74	-113.43 ± 2.07
6650047986394047104	2457970.9907	2457971.0324	0.5474	0.4544	3140 ± 47	-55.55 ± 0.46	-64.54 ± 2.51
6664639188589394688	2457948.0900	2457948.1316	0.2341	0.0055	2639 ± 106	-26.87 ± 0.77	-19.91 ± 1.06
6665135721170434816	2457948.0900	2457948.1317	0.4507	0.3316	1819 ± 46	-40.44 ± 1.20	-40.07 ± 2.13
6674570703462167680	2458001.9963	2458002.0379	0.9207	0.8198	3289 ± 159	47.83 ± 1.53	24.93 ± 2.58
6679308288613240064	2457647.9346	2457647.9762	0.4469	0.3382	4425 ± 387	-104.88 ± 2.20	-104.47 ± 3.15
6681635649786400384	2457209.2180	2457209.2596	0.8397	0.6984	3928 ± 341	-45.60 ± 0.68	-62.26 ± 1.88
6681944303315818624	2457209.2179	2457209.2596	0.0427	0.9499	3899 ± 62	-57.32 ± 1.45	-26.67 ± 2.71
6694638955332768512	2457539.2330	2457539.2747	0.6412	0.3951	3167 ± 204	19.11 ± 0.92	12.32 ± 1.41
6698926702788332416	2457881.2933	2457881.3350	0.5224	0.3225	1678 ± 47	-43.14 ± 0.63	-48.34 ± 1.68
6730211038418525056	2457945.0908	2457945.1325	0.7048	0.5919	841 ± 13	-76.44 ± 1.89	-92.12 ± 2.64
6768220266332023040	2457303.8817	2457303.9233	0.4975	0.3341	2477 ± 139	-195.92 ± 1.02	-198.94 ± 1.93
6795546531894178816	2458029.9037	2458029.9454	0.1195	0.0163	3321 ± 212	-210.85 ± 2.50	-182.10 ± 3.13

Table A3. Dynamic properties of the total sample of RRLs. This excerpt is shown for guidance, the entire table is made available through CDS.

Gaia DR3 ID	V_x	V_y [km/s]	V_z	L_z	L_{perp} [kpc km/s]	E [km ² /s ²]	λ_z	Stream
15489408711727488	26.11	-28.13	-13.22	-237	130	-180178	-0.19	ThII
80556926295542528	79.69	170.59	-16.25	1663	336	-156398	0.87	-
144809087288307584	-61.04	162.08	-12.61	1537	122	-159975	0.86	-
182142003881848832	-39.07	246.99	7.12	2201	63	-147465	0.98	-
234108363683247616	5.83	240.99	-14.35	2059	126	-151882	1.00	-
289662047665943552	0.79	243.46	17.66	2110	148	-150013	0.99	-
294072906063827072	-165.64	-122.33	2.47	-1120	103	-160181	-0.63	-
305829816397138688	-26.91	127.94	-9.26	1198	142	-164522	0.73	-
315028326379733760	-149.65	-30.00	11.23	-505	224	-163751	-0.30	ThI
317254635562605184	-95.21	34.67	-41.98	202	548	-164905	0.12	GSE

Table A4. Average abundances of RRLs in bins of λ_z .

λ_z	[Fe/H] _{HR}		[Fe/H] _{LR}		[Ca/Fe]		[Y/Fe]		[Ba/Fe]	
	n	mean±std	n	mean±std	n	mean±std	n	mean±std	n	mean±std
$\lambda_z > 0.8$	66	-0.714 ± 0.561	116	-0.786 ± 0.605	62	0.046 ± 0.195	11	-0.249 ± 0.321	12	-0.234 ± 0.268
$0.25 < \lambda_z \leq 0.8$	56	-1.426 ± 0.442	129	-1.472 ± 0.440	52	0.215 ± 0.170	17	-0.004 ± 0.315	19	-0.149 ± 0.290
$-0.25 < \lambda_z \leq 0.25$	80	-1.626 ± 0.288	214	-1.645 ± 0.321	71	0.314 ± 0.112	18	0.085 ± 0.283	25	-0.027 ± 0.268
$\lambda_z \leq -0.25$	29	-1.673 ± 0.393	73	-1.734 ± 0.408	28	0.283 ± 0.144	6	0.219 ± 0.306	7	0.040 ± 0.275

Table A5. Line list for atomic transitions employed in the present study.

Wavelength (Å)	Species	E.P. (eV)	log gf (dex)
5711.088	Mg 1	4.35	-1.742
5690.425	Si 1	4.93	-1.802
5708.410	Si 1	4.95	-1.370
5721.021	Si 1	5.86	-0.852
5772.146	Si 1	5.08	-1.643
5793.073	Si 1	4.93	-1.894
6555.462	Si 1	5.98	-0.886
5857.451	Ca 1	2.93	0.240
6493.781	Ca 1	2.52	-0.109
4727.413	Fe 1	3.69	-1.083
4736.774	Fe 1	3.21	-0.674
4798.265	Fe 1	4.19	-1.174
4799.845	Fe 1	4.39	-2.322
4878.210	Fe 1	2.89	-0.887
4891.490	Fe 1	2.85	-0.111
4892.861	Fe 1	4.22	-1.290
5655.459	Fe 1	5.03	-0.436
5662.532	Fe 1	4.18	-0.447
5679.025	Fe 1	4.60	-0.820
5686.531	Fe 1	4.55	-0.445
5701.537	Fe 1	2.56	-2.193
5706.004	Fe 1	4.61	-0.460
5715.083	Fe 1	4.28	-0.970
5717.836	Fe 1	4.28	-0.990
5753.123	Fe 1	4.26	-0.623
5762.989	Fe 1	4.21	-0.360
5775.080	Fe 1	4.22	-1.126
5780.566	Fe 1	3.24	-2.540
5816.366	Fe 1	4.55	-0.601
6494.979	Fe 1	2.40	-1.268
6592.912	Fe 1	2.73	-1.473
6593.868	Fe 1	2.43	-2.420
6609.107	Fe 1	2.56	-2.691
6633.751	Fe 1	4.56	-0.799

Table A5 – continued

Wavelength (Å)	Species	E.P. (eV)	log gf (dex)
6663.441	Fe 1	2.42	-2.473
6677.982	Fe 1	2.69	-1.418
4893.818	Fe 2	2.83	-4.267
5651.523	Fe 2	10.63	-0.615
5806.822	Fe 2	10.68	-1.324
6495.212	Fe 2	11.09	0.031
6516.077	Fe 2	2.89	-3.31
4883.682	Y 2	1.08	0.190
4900.119	Y 2	1.03	0.030
5853.668	Ba 2	0.60	-0.907
6496.897	Ba 2	0.60	-0.407

¹Department of Physics, University of Rome Tor Vergata, via della Ricerca Scientifica 1, 00133 Rome, Italy²INAF – Osservatorio Astronomico di Padova, vicolo dell' Osservatorio 5, 35122 Padova, Italy³Department of Physics and Astronomy, Monash University, Clayton, VIC 3800, Australia⁴ARC Centre of Excellence for All Sky Astrophysics in 3 Dimensions (ASTRO 3D), Australia⁵Max Planck Institute for Astronomy, Königstuhl 17, 69117 Heidelberg, Germany⁶INAF – Osservatorio Astronomico di Roma, via Frascati 33, Monte Porzio Catone, Italy⁷Department of Astrophysics, Türkenschanzstraße 17 (Sternwarte), 1180 Wien, Austria⁸Space Science Data Center - ASI, via del Politecnico s.n.c., I-00133, Rome, Italy⁹Department of Astronomy and McDonald Observatory, The University of Texas, Austin, TX 78712, USA¹⁰INAF – Osservatorio di Astrofisica e Scienza dello Spazio di Bologna, via P. Gobetti 93/3, 40129 Bologna, Italy¹¹Institut d'Astronomie et d'Astrophysique, Université libre de Bruxelles, CP 226, Boulevard du Triomphe, 1050 Brussels, Belgium

¹²*Research School of Astronomy and Astrophysics, The Australian National University, Canberra ACT2611, Australia*

¹³*School of Mathematical and Physical Sciences, Macquarie University, Balaclava Road, Sydney, NSW 2109, Australia*

¹⁴*Astrophysics and Space Technologies Research Centre, Macquarie University, Balaclava Road, Sydney, NSW 2109, Australia*

¹⁵*International Space Science Institute–Beijing, 1 Nanertiao, Zhongguancun, Beijing 100190, China*

¹⁶*Konkoly Observatory, HUN-REN Research Centre for Astronomy and Earth Sciences, Konkoly Thege Miklós út 15-17., H-1121, Hungary*

¹⁷*CSFK, MTA Centre of Excellence, Budapest, Konkoly Thege Miklós út 15-17., H-1121, Hungary*

¹⁸*ELTE Eötvös Loránd University, Institute of Physics and Astronomy, Budapest 1117, Pázmány Péter sétány 1/A, Hungary*

¹⁹*Lund Observatory, Department of Geology, Sölvegatan 12, SE-22362 Lund, Sweden*

²⁰*Department of Physics and Astronomy, Dartmouth College, Hanover, NH03755, USA*

²¹*INAF – Osservatorio Astronomico di Capodimonte, salita Moiariello 16, 80131, Naples, Italy*

²²*Department of Physics, Florida State University, 77 Chieftain Way, Tallahassee, FL32306, USA*

²³*Gemini Observatory/NSF’s NOIRLab, 670 N.A’ohokuPlace, Hilo, HI96720, USA*

²⁴*Department of Astronomy, School of Science, The University of Tokyo, 7-3-1 Hongo, Bunkyo-ku, Tokyo 113-0033, Japan*

²⁵*Laboratory of Infrared High-resolution Spectroscopy, Koyama Astronomical Observatory, Kyoto Sangyo University, Kyoto 603-8555, Japan*

²⁶*IAC – Instituto de Astrofísica de Canarias, Calle Vía Lactea s/n, E-38205 La Laguna, Tenerife, Spain*

²⁷*Departamento de Astrofísica, Universidad de La Laguna, E-38206 La Laguna, Tenerife, Spain*

²⁸*Department of Physics and Astronomy, Iowa State University, Ames, IA50011, USA*

²⁹*Center for Astrophysical Sciences and Department of Physics and Astronomy, The Johns Hopkins University, Baltimore, MD 21218, USA*

³⁰*Université de Nice Sophia-Antipolis, CNRS, Observatoire de la Côte d’Azur, Laboratoire Lagrange, BP4229, F-06304 Nice, France*

³¹*INAF – Istituto di Radioastronomia, via Gobetti 101, 40129 Bologna, Italy*

³²*Institute for Astronomy, University of Hawaii at Manoa, 2680 Woodlawn Dr, Honolulu, HI 96822, USA*

³³*Universitäts-Sternwarte, Fakultät für Physik, Ludwig-Maximilians Universität München, Scheinerstraße 1, D-81679 München, Germany*

³⁴*Sydney Institute for Astronomy, School of Physics, A28, The University of Sydney, NSW 2006, Australia*

³⁵*Faculty of Mathematics and Physics, University of Ljubljana, Jadranska 19, 1000 Ljubljana, Slovenia*

³⁶*Department of Astronomy, Stockholm University, AlbaNova Research Centre, SE-10691, Stockholm, Sweden*

³⁷*School of Physics, UNSW, Sydney, NSW 2052, Australia*

This paper has been typeset from a $\text{\TeX}/\text{\LaTeX}$ file prepared by the author.